Planetary and Space Science 218 (2022) 105504

Contents lists available at ScienceDirect

Planetary and Space Science

journal homepage: www.elsevier.com/locate/pss

Calibration of the NOMAD-UVIS data

Yannick Willame [a,*], Cédric Depiesse [a], Jonathon P. Mason [b], Ian R. Thomas [a], Manish R. Patel [b,c], Brijen Hathi [b], Mark R. Leese [b], David Bolsée [a], Michael J. Wolff [d], Loïc Trompet [a], Ann Carine Vandaele [a], Arianna Piccialli [a], Shohei Aoki [a,e], Bojan Ristic [a], Eddy Neefs [a], Bram Beeckman [a], Sophie Berkenbosch [a], Roland Clairquin [a], Arnaud Mahieux [a,h], Nuno Pereira [a], Séverine Robert [a], Sébastien Viscardy [a], Valérie Wilquet [a], Frank Daerden [a], José Juan Lopez-Moreno [f], Giancarlo Bellucci [g]

[a] Royal Belgian Institute for Space Aeronomy, BIRA-IASB, 3 Avenue Circulaire, 1180, Brussels, Belgium
[b] School of Physical Sciences, The Open University, Milton Keynes, UK
[c] Space Science and Technology Department, Science and Technology Facilities Council, Rutherford Appleton Laboratory, Oxfordshire, UK
[d] Space Science Institute, Boulder, CO, USA
[e] Institute of Space and Astronautical Science (ISAS), Japan Aerospace Exploration Agency (JAXA), Sagamihara, Japan
[f] Instituto de Astrofisica de Andalucía/CSIC, Granada, Spain
[g] Istituto di Astrofisica e Planetologia Spaziali, INAF, Rome, Italy
[h] The University of Texas at Austin, Austin, TX, USA

A B S T R A C T

The Ultraviolet and VIsible Spectrometer (UVIS), covering the 200–650 nm range, is one of three spectrometers that comprise the NOMAD instrument on the ExoMars 2016 Trace Gas Orbiter (TGO). UVIS can operate in solar occultation, nadir and limb viewing mode and was designed to monitor ozone and aerosols in the Martian atmosphere. Here, we describe the calibration procedure to convert the UVIS raw data into a calibrated data product ready for scientific exploitation. The calibration includes the CCD offset and dark current subtraction, the wavelength assignment, the noise identification and removal, the smearing removal, and the radiance or transmittance conversion. A straylight correction, critical for some parts of the UVIS spectral range, is also applied during the data reduction process, which is described in more detail in two companion papers [Mason et al., 2022; Depiesse et al., In prep] corresponding to two different and independent methods giving consistent results. The solar occultation observations are converted into transmittance and are therefore self-calibrating, while nadir and limb measurements require an absolute radiometric calibration. A comparison with coincident nadir MRO/MARCI measurements is provided as a final validation and generally shows a ±10% agreement on the radiances measured by both instruments.

1. Introduction

The Nadir and Occultation for MArs Discovery (NOMAD) instrument onboard ExoMars 2016 Trace Gas Orbiter (TGO) was designed to study the composition of the Martian atmosphere with a particular focus on trace gases and aerosols [Neefs et al., 2015; Robert et al., 2016; Vandaele et al., 2018]. TGO has been in orbit around Mars since 2016, with the nominal science mission beginning in April 2018 after a period of aerobraking to achieve the final science orbit. The NOMAD spectrometer suite is composed of three channels. Two channels are infrared (IR) spectrometers and were designed to operate under a specific geometry: The “Solar Occultation” channel (SO), and the “Limb, Nadir and Occultation” channel (LNO). The third channel, UVIS, operates in three viewing geometries: solar occultation, nadir and limb in order to achieve its main scientific aims; to study and to monitor atmospheric ozone, dust, and ice aerosols in the Martian atmosphere. A detailed description of the UVIS instrument is provided by [Patel et al., 2017].

In this paper we describe the calibration process to convert UVIS raw data to fully calibrated data (radiance or transmittance) ready for science analysis. Section 2 gives a description summary of the instrument and its characteristics. In Section 3, we present the viewing modes and their associated measurement characteristics. Section 4 describes the calibration process from raw data to level 1. Finally, in Section 5, we present a radiometric comparison of the UVIS calibrated data with measurements from the Mars Color Imager (MARCI) instrument [Bell et al., 2009] aboard the Mars Reconnaissance Orbiter (MRO), as validation of the calibration process.

* Corresponding author.
E-mail address: yannick.willame@aeronomie.be (Y. Willame).

https://doi.org/10.1016/j.pss.2022.105504
Received 3 January 2022; Received in revised form 30 April 2022; Accepted 3 May 2022
Available online 13 May 2022

2. Instrument description and characteristics

The optical design of UVIS is based on a conventional Czerny-Turner configuration spectrometer. The instrument is composed of two parts, the spectrometer itself, and the entrance optics that collect light from the UVIS telescopes apertures. There are two telescopes for UVIS, one for the nadir (also used for limb measurements) and one for the solar occultation mode (often referred hereafter just as occultation). For a more detailed description of the UVIS design the readers are referred to [Patel et al., 2017] and for its radiometric performance to [Vandaele et al., 2015].

As shown in Fig. 1, the light passing through the entrance aperture is collected by a parabolic mirror for the nadir entrance, or by a flat mirror followed by a parabolic mirror when working in occultation. The parabolic mirror concentrates the light into the optical fiber(s): due to the difference of intensity, the occultation channel contains one optical fiber to collect the incoming light, while the nadir channel is composed of a bundle of 19 fibers mounted in a circular plan at the telescope entrance and in a vertical plan at the exit in front of the spectrometer. The optical fiber for a selected channel is moved in front of spectrometer's entrance by the selector mechanism, allowing light from that channel to enter the spectrometer. The selector mechanism has three possible positions, occultation, nadir and a third, non-illuminated, position (referred to as "dark") where measurement of the "dark" background noise can be performed.

Once the light passes through the selector mechanism, it enters the spectrometer aperture via a slit and reflects on a collimating mirror before reaching the diffraction grating, where the spectral decomposition occurs. After decomposition, a focusing mirror is used to re-focus the same spectral components of light on the detector to record the spectral intensity. A high-pass filter is coated on the longer wavelength half of the detector to reject the second order of shorter wavelength radiation.

UVIS covers the spectral range from 200 to 650 nm with a resolution ranging between 1.2 nm at the shortest wavelengths and 1.7 nm at the longest wavelengths. The detector is a CCD with 256 rows (spatial direction) of 1024 pixels along the spectral direction and which will be referred hereafter as the "spectral pixels". The field of view (FOV) of the occultation channel is 2 arcmin corresponding to an instantaneous FOV of about 1 km at tangent altitude, while the nadir channel has a 43 arcmin circular FOV, corresponding to a 5 km diameter instantaneous footprint on the planet surface in nadir viewing, and to about 20 km at tangent altitude for limb observations.

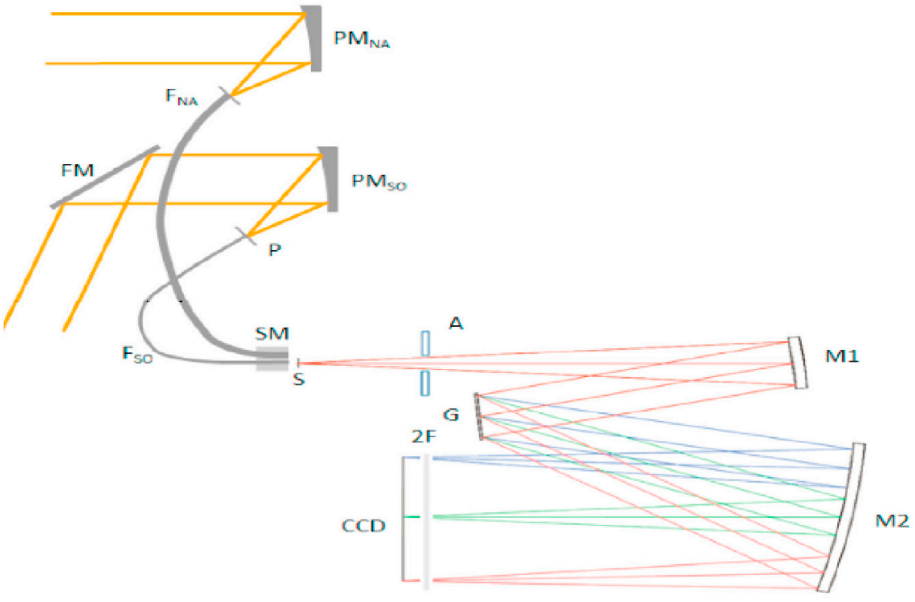

Fig. 1. Schematics of the UVIS instrument reproduced from [Vandaele et al., 2015]: the entrance optics for nadir observations (NA) with the parabolic mirror (PM$_{NA}$) and the bundle of fibers (F$_{NA}$), the entrance optics for solar occultation observations (SO) with the flat mirror (FM) located in the periscope, the parabolic mirror (PM$_{SO}$), the pinhole (P) and the optical fiber (F$_{SO}$); the selector mechanism (SM); the spectrometer with the entrance slit (S), the aperture (A), the collimating mirror (M1), the diffraction grating (G), the focusing mirror (M2), the 2nd order filter (2F) and the detector (CCD).

3. Measurements and data

In this section, we describe the types of observations performed by UVIS and how the data are recorded and organized. The data are organized in files containing each several consecutive measurements acquired with the same observation mode, i.e. nadir (dayside/nightside), limb (dayside/nightside) or occultation. The raw data files recorded on board are transmitted back to Earth, where they are converted and stored under hdf5 format data files to be calibrated. The calibration process undergoes several steps, starting with the addition of the geometry characteristics, followed by the data reduction described in detail in the present paper.

Prior to detailing the calibration, we introduce the way the data are recorded on board: We explain first the binning and truncation possibilities of the CCD in Section 3.1 and describe the CCD readout in Section 3.2. The different viewing modes and their associated characteristic CCD frames are then described in Section 3.3. Finally, a description of the different measurements composing a data file is given in Section 3.4.

3.1. CCD frame, onboard data binning and truncation

Each UVIS observation records a CCD frame that generally contains the UV–visible range 200–650 nm. An example of typical raw CCD frames for a nadir and an occultation observation is shown in Fig. 2.

Recording CCD frames in such a manner results in large data volumes, as such UVIS represents the majority of the NOMAD data volume to be transmitted back to Earth. As the data volume allowance varies during the mission, the UVIS output is modified to lower its data volume requirements but still achieve the frame output critical for the calibration process. The UVIS CCD can operate with different binning and truncation modes in order to reduce the quantity of data recorded (one setup choice per file):

- Vertical truncation: A vertical truncation is performed to reduce the number of transmitted rows. Only the CCD rows necessary for an accurate data treatment are kept, all the other rows are discarded. The part of the CCD which is kept is called hereafter the region of interest (ROI). The ROI includes: the "light" region (LR) illuminated by the desired incoming light; and the "non-light" region (NLR), located on each side (top and bottom) of the LR, that is not illuminated by the desired incoming light. The NLR contains however straylight (as does the LR) and is useful for the straylight removal process. The

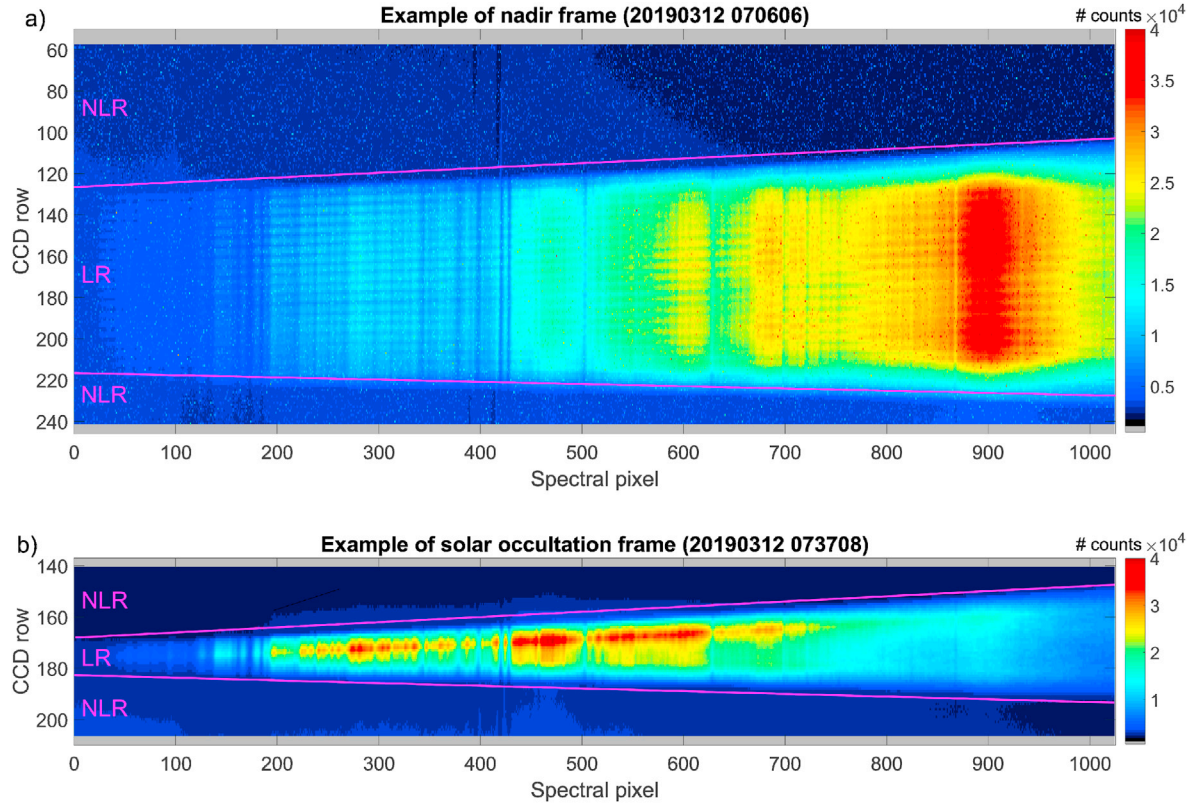

Fig. 2. Examples of UVIS CCD recorded raw frames for (a) nadir and (b) solar occultation observations. Spectral pixel #1 corresponds to the UV (around 200 nm), while pixel 1024 is a visible wavelength (around 650 nm). The typical ROI for each observation mode is represented by colored rows while the grey parts present at the very top and bottom of each frame represent the limits of discarded rows from the vertical truncation. The limits between the illuminated "light" region (LR) and the non-illuminated "no light" regions (NLR) are delimited by the purple lines. No horizontal binning was applied for these two measurements.

delimitation of the ROI, LR and NLR are displayed in Fig. 2. Another advantage of the vertical truncation is the reduction of the CCD readout time, as will be discussed in the next section.

- Horizontal truncation: Truncating a part of the spectral range is sometimes used to record measurements with a longer integration time in the UV, where the signal is lower (cf. Fig. 2), to increase the Signal-to-Noise Ratio (SNR). This mode is not nominal and not often used.
- Vertical binning: It is possible to bin all the rows of the ROI during the readout of the CCD in order to transmit only one single binned row instead of a frame. This recording mode significantly degrades the data treatment, preventing the straylight correction and the bad pixels' removal. This mode was used at the beginning of the mission but was abandoned as a viable observation option due to the presence of severe straylight issues in the binned spectra.
- Horizontal binning: Binning spectral pixels is the preferred solution to reduce the data volume transmission when necessary. Nominally, the instrument operates without spectral binning but when necessary (low data rate conditions) the pixels of a row can be binned in sets of four or eight. This mode degrades the spectral resolution and the identification of the bad pixels.

3.2. CCD readout

The CCD readout process is important as the selector mechanism is kept in the same position during consecutive science measurements and the CCD is therefore continually exposed to input signal during the readout. The readout process starts with the vertical truncation: all bottom rows outside ROI are flushed and the ROI is shifted down by the same number of rows. The readout of the ROI is then performed row by row: reading the very bottom row then shifting down the remaining ROI by one row. This process is performed iteratively until the whole ROI is read and takes about 10 ms per row.

Practically, it means that using a larger truncation with a smaller ROI will prevent signal contamination during the readout process: occultation observations are recorded in that way (see details in Section 3.3.1). Whereas frames recorded using a smaller truncation with a larger ROI will suffer from signal contamination during readout, a problem evident in nadir and limb measurements (see Section 3.3.2 and 3.3.3).

3.3. Viewing geometries and CCD frames

3.3.1. Solar occultation

A solar occultation observation involves pointing the UVIS occultation telescope towards the Sun such that the UVIS-Sun line of sight intersects with the Martian atmosphere allowing measurement of atmospheric extinction at different altitudes. An occultation file contains a single occultation observation that groups a set of occultation measurements corresponding to different tangential altitudes from top to bottom for an ingress (or inversely for an egress) in the atmosphere. The vertical resolution between two consecutive measurements usually varies between 0.2 and 1.4 km (and 0.7–4.4 km until mid-February 2019).

The calibrated spectra from this viewing mode are converted into transmittances (see Section 4.9.1): all spectra are divided by a reference solar spectrum, which is obtained by averaging several spectra measured during the same observation above the top of the atmosphere where no extinction occurs. Those spectra are therefore relative and "self-calibrated" (from a radiometric perspective).

A recorded frame of a solar occultation observation is shown in the bottom panel of Fig. 2. The ROI ranges from row 141 to 206 (66 rows retained) and as of August 2020 the ROI was increased from row 136 to 206 (71 rows retained) to allow for calibration improvements. The ROI is

thus shifted down by 140 rows (135 rows) to perform the readout. As a result of the vertical truncation, the ROI is fully shifted into the non-illuminated bottom part of the CCD while being read and is therefore not contaminated by additional illumination. The change in the width of the ROI increased the CCD readout time from 720 ms to 770 ms which only marginally decreased the vertical resolution of occultation observations. In occultation the width of the LR varies from about 15 rows at the UV end and increases to about 50 rows at the visible end. Occultation measurements are typically recorded with an integration time (IT) of 45 or 75 ms. When added to the CCD readout and the data transmission time to the onboard computer, this gives a total measurement cadence of approximately 1.1 s. It is this measurement cadence and the total observation duration that determines the vertical resolution of an occultation observation.

3.3.2. Nadir

A dayside nadir measurement consists in pointing down at the planet surface, i.e. with the line of sight following the normal to Mars areoid, to record the solar radiation backscattered by the atmosphere and/or the surface. It permits assessment of the absorption and scattering of the atmosphere integrated over the total atmospheric height (also called atmospheric column) and/or the surface reflectance with a good spatial resolution over localized areas on the planet. The footprint on the Martian surface represents a stadium shape of about 5 km cross-track and 20–100 km along-track, depending on the integration time.

Nadir nightside measurements are also performed occasionally, the geometry is the same but the instrument then records the light emitted by the atmosphere. These observations are not frequent since emissions are very weak in the UV–visible.

Nadir observations require an absolute radiometric conversion (described in Section 4.9.2), as no solar reference measurement is recorded in this mode.

A recorded frame of a dayside nadir observation is shown in the top panel of Fig. 2. The ROI generally comprises 184 CCD rows from row 58 to 241 (189 rows [58–246] from August 2020). The LR spreads on about 100 rows at the UV end and increases to about 130 rows at the visible end. Nadir measurements are typically recorded with integration time of 5–20 s, and have a CCD readout time of about 2 s. In this case, the ROI is thus shifted down by only 57 rows to perform the readout (as a result of the vertical truncation), implying that the upper part of the ROI is still illuminated while being read. This is called the "smearing" effect and has to be taken into account and corrected during the calibration process (detailed in Section 4.5).

3.3.3. Limb

A limb measurement consists in pointing the nadir telescope toward the atmospheric limbs in front of deep space in order to record emissions (dayside/nightside) and/or scattered solar light (dayside) at different altitudes. A limb observation contains a set of these altitude measurements from above the top of the atmosphere down to generally 30–60 km altitude. Nightside limb measurements can also be performed, but are not frequent due to the weak signal measured in this configuration.

Limb measurements use the same ROI characteristics as the nadir measurements described in previous Section 3.3.2.

3.4. Science, dark and bias measurements

An observation file contains three types of measurements. It always starts and ends with a combination of two housekeeping measurements: a "bias" followed by a "dark" measurement, see below for description. In between, the core of the file contains all the "science" measurements, i.e. those requiring calibration and used for the study of Mars. Early in the mission, several dark measurements were also recorded in the core when using the nadir channel but it was stopped to extend the lifetime of the selector mechanism.

"Bias" and "dark" measurements are used for calibration purpose and are recorded without illumination, i.e. with the selector mechanism in "dark position", preventing light from reaching the spectrometer and the detector. A bias measurement is recorded with a 0 ms integration time and is used for the read noise calculation (see Section 4.10.1). While the dark measurements are recorded with the same integration time as the "science" measurements and are used to estimate the accumulated dark charge to be subtracted.

"Science" measurements are recorded with the selector mechanism is in either nadir or occultation position and must be seen as a two-step process. First, during the exposure time, the LR of the frame receives the signal from the desired light source (Mars/Sun) but also straylight and dark charges due to the dark current. These two last contributions need to be removed.

Second, during the readout process, some additional contributions are recorded. For occultations, NLR straylight and dark charges need to be considered. In nadir, the same applies for the part of the "shifted" ROI that lies outside of the LR during the readout. However, the part of the "shifted" ROI, that still lies in the LR, acquires additional Mars/Sun signal and LR straylight. These additional straylight and signal components are related to the "smearing" effect, which must be corrected for in the nadir/limb observations. This effect is negligible for occultation observations.

The science measurements require a complete calibration process divided in the following steps: 1) non-linearity correction 2) offset bias removal; 3) dark current removal; 4) bad pixel identification; 5) smearing removal; 6) wavelength assignment 7) straylight removal; 8) vertical binning (on the LR rows to increase the SNR); 9) radiance (nadir/limb) or transmittance (occultation) conversion.

4. Data calibration

We consider here the calibration of a raw "science" CCD frame $Y_{raw}(w,r,i)$. The indices "w" and "r" refer respectively to the "wavelength" (i.e. spectral pixel) and "row" index of the CCD frame, while "i" is the "measurement" index in the file to calibrate. The shortened notation $Y_{raw}(w,r)$ will be often used when referring to a CCD frame for reading clarity when the reference to the measurement index is not needed.

4.1. Linearity correction

The first step consists in checking the values recorded by each pixel of the CCD to identify which are in the non-linear regime. Indeed the linear relation for the CCD between electrons recorded and the number of photons reaching it is valid until a certain threshold, accumulating from there the electrons with a decreasing rate. The way to study the (non-) linearity is usually performed using measurements at different integration times (IT) using the same light source. Such measurements were performed with the nadir channel during the ground calibration campaign for 6 ITs between 0.5 and 12 s. Unfortunately the longest IT is not sufficient to study the linearity on the full capacity range of the CCD. The theoretical full-well capacity of our CCD is 65,536 counts (2^{16}) while the measurements of the longest IT only reach values of about 43,000 counts. Nevertheless these measurements were used to verify the linearity until 43 k counts.

In order to extend the study to higher values, we used the direct Sun measurements recorded in occultation at the beginning of the mission in June 2018. Several occultations using 4 different ITs (30, 45, 75 and 100 ms) were recorded in a short time period (12 consecutive days). The principle was first to build a frame for each IT by averaging together several direct Sun measurements (i.e. a relatively constant source). The 100 ms frame reaches the full-well capacity for certain pixels, which allows to study the (non-)linearity of the CCD on its full capacity range. The (non-)linearity curve is shown in Fig. 3. It was derived by identifying and averaging together all the pixels with similar values in the 100 ms frame and compare it to the average obtained from the same pixels of the other IT frames. The results from the three lower ITs were fitted to determine the linear slope and quantify the deviation of the 100 ms

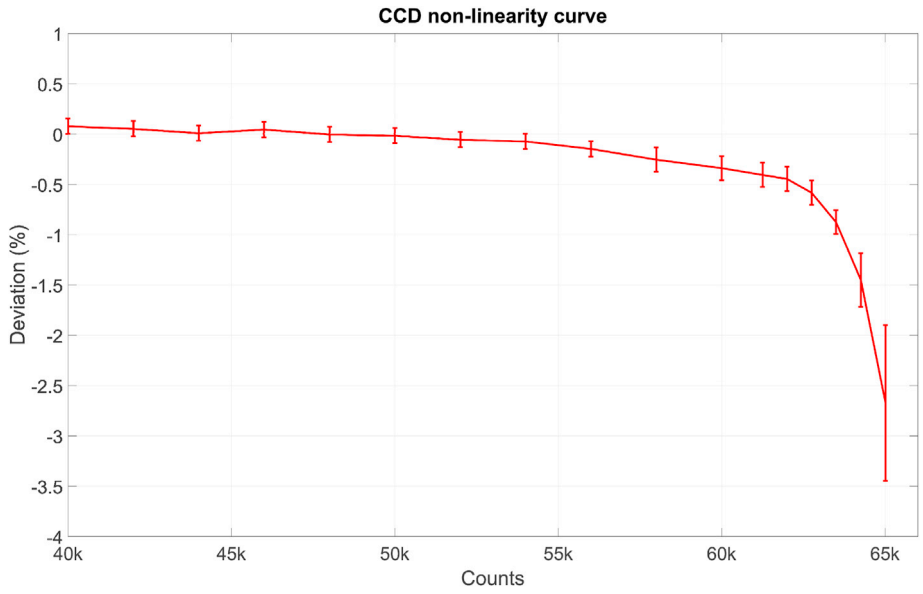

Fig. 3. Deviation from the linear electron accumulation of the UVIS CCD. The UVIS shows a linear regime until about 54 k accumulated counts then enters in the non-linear regime. This curve is used to correct the raw UVIS data in the non-linear regime (see details in the text).

results.

The curve in Fig. 3 is used to correct part of the UVIS data found in the non-linear regime.

All the raw pixels found in the non-linear regime below 1% deviation (i.e. between about 54 k and 63.5 k) are corrected for the deviation. About 2% of the recorded frames are affected by pixels in this non-linear regime, both for nadir daysides and occultations.

While the raw pixels with values larger than 63.5 k are not corrected, they are flagged as saturated pixels to be discarded (cf. Section 4.4). They represent respectively about 5.7% and 1% of the nadir daysides' and occultations' frames. Note that the presence of saturated pixels in a frame does not jeopardize its calibration as it only concerns the part(s) of the frame where the signal is the highest (see Fig. 2). The rest of the frame remains perfectly useable to pursue the calibration process.

4.2. Offset bias removal

The removal of the offset bias which is calculated for each CCD row then subtracted from the raw frame. The UVIS CCD has sixteen virtual pixels at the end of each CCD row, called the overscan pixels, that are not illuminated and, being virtual, do not accumulate charge from thermal dark current. The offset bias $O_B(r)$ is obtained by calculating the mean signal over the last eight of these overscan pixels. The first eight overscan pixels are not used as they may suffer from signal leaks from the effective part of the CCD. The frame corrected for the offset $Y_{Off}(w,r)$ is thus obtained from Y_{rawLin} (i.e. Y_{raw} after potential non-linearity corrections, as described in Section 4.1):

$$Y_{Off}(w,r) = Y_{rawLin}(w,r) - O_B(r)$$

4.3. Dark current removal

The next step in the calibration process is to estimate the charge accumulated from thermally generated dark current (DC) and remove it from the bias offset corrected frame (Y_{Off}). The frame corrected for dark current (Y_{DC}) is calculated by subtraction of the DC correction frame (Y_{dark}):

$$Y_{DC}(w,r) = Y_{Off}(w,r) - Y_{dark}(w,r)$$

The DC correction frame $Y_{dark}(w,r)$ is obtained using a combination of the 2 dark frames, recorded before and after the considered measurement, respectively noted as $Y_{dark1}(w,r)$ and $Y_{dark2}(w,r)$:

$$Y_{dark}(w,r,i) = (1-k_i)\, Y_{dark1}(w,r) + k_i\, Y_{dark2}(w,r) \quad (1)$$

where k_i is a weighting fraction for the ith measurement within an occultation or nadir observation and is calculated using the dark current vs detector temperature function "DC(T)". DC(T) was found by fitting an exponential function to the measured DC at different CCD temperatures, over the 2018 period. The DC temperature dependence and the DC(T) best fit are shown in Fig. 4a.

For each UVIS observation, the CCD temperature is recorded at the end of each measurement at a resolution of 0.39 °C. The coarse temperature resolution was found to be insufficient for accurate DC determination and therefore an estimate of the 'true' CCD temperature, $T_{fit}(m)$, was found by fitting the recorded CCD temperatures with a 6th order polynomial, as shown in Fig. 4b. Combining T_{fit} and DC(T), the weighting fraction for ith measurement is calculated as follows:

$$k_i = \frac{DC(i) - DC(i_{dark1})}{DC(i_{dark2}) - DC(i_{dark1})}$$

where we used a shortened notation for clarity: DC(i) stands for $DC(T_{fit}(i))$; i_{dark1} and i_{dark2} are the measurements indices for the two dark observations. An example of the estimated dark current for a CCD row in a science measurement, obtained from Equation (1) in Section 4.3 is shown in Fig. 5.

4.4. Bad pixel flagging

Bad pixels must be identified in order to not jeopardize the quality of the data calibration. They must be discarded before the straylight removal process (Section 4.7) and the binning of the LR CCD rows (Section 4.8).

Bad pixels refer here to several types of issues. (1) saturated pixels: Pixels which are in the non-linearity regime of the CCD above 63.5 k counts (in the raw data, see Section 4.1). (2) hot pixels: Pixels which do not respond linearly in a recurrent way. And (3) anomalous pixels: Pixels which show a one-time unexpected behavior such as a cosmic ray hitting the detector and contaminating one or several adjacent pixels on the CCD.

Hot pixels: The detection of hot pixels is performed using the dark frame measurements within the considered observation. The DC signal

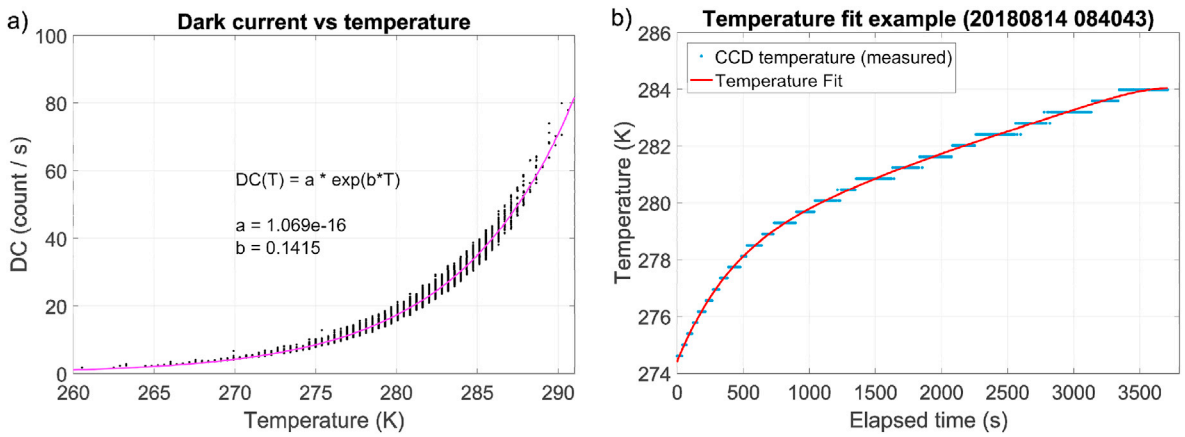

Fig. 4. a): Dark current as function of CCD temperature. The black dot corresponds to the averaged dark current measured on the whole CCD frame. The pink line shows the derived exponential DC(T) function derived using the data from 2018 measurements. b) Example of the CCD temperature fit for a nadir observation.

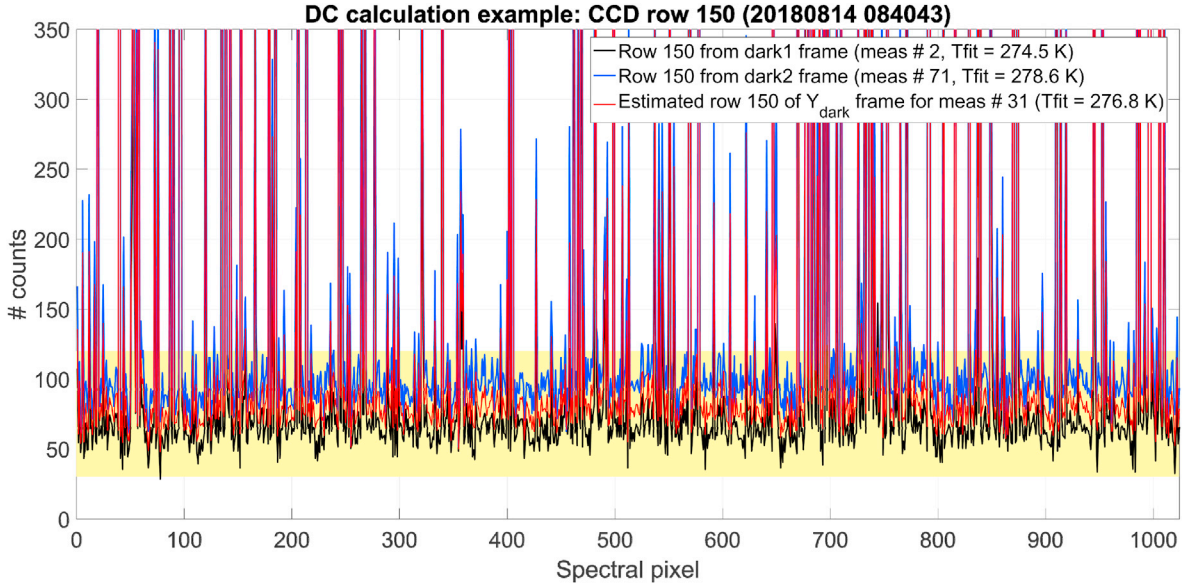

Fig. 5. Example of an estimated dark current spectrum (red line) for the CCD row 150 of a nadir observation using the previous and next dark measurements (black and blue lines). We note that the dark spectra are relatively constant here with a "normal" count level around 50–100 counts (highlighted in yellow area) with mostly small variations (of about some counts) due to the thermal and readout noises. The large spikes (of 100s/1000s of counts) correspond to hot pixels (discussed in Section 4.4).

shows relatively small variations due to the thermal and readout noises, as highlight in the yellow band of Fig. 5. The pixels with larger deviations from the dark signal are potential hot pixels. To find them, we calculate the median M(r) and standard deviation Std(r) on all the pixels for each CCD row. The "divergent" pixels that differ significantly from the median are identified for each row by: $Y_{raw}(w,r) - M(r) > k_{hot}\ Std(r)$.

This process is iterated several times with the M(r) and Std(r) updated at each iteration, discarding all the "divergent" pixels identified at previous iteration for the calculation of the next one. The number of iterations (typically between 2 and 4) and the k_{hot} factor (typically between 2.5 and 4) were arbitrarily chosen, using a subset of observations at the beginning of the mission, by iterative tuning and visual approval of the noise removed dark spectra. We have chosen one set of values for each type of measurement, which was defined depending on how strict the "divergent" pixel detection is required. For instance, the number of divergent pixels is relatively important in nadir/limb frames but (almost) not present in occultation frames. It can be seen comparing the frames of Fig. 2, that numerous brighter spots are present in the nadir frame, while these same bright spots are not observed in the occultation frame. Also, the lower the intensity of the incoming signal, the more important the impact that these divergent pixels have. Therefore, occultations require a less constrained detection, as the signal is usually strong and the frames are not affected by divergent pixels. Medium constrain criteria are used for dayside nadir, which suffers from divergent pixels and usually has a medium to large signal intensity, while a stricter detection is applied to limb and nightside measurements, also affected by divergent pixels but for which the signal is low.

The hot pixels, to be removed, are identified as the divergent pixels that were found in both dark frames of the observation.[1] The proportion of hot pixels usually found in a frame represents less than 0.1% for occultations, 8–11% for nadir dayside measurements and 14–17% for limb and nightside measurements.

[1] Except at the beginning of the mission when more than two dark frames were recorded per observation. Hot pixels were then identified if the detection had occurred in more than 50% of the dark frames (the 50% threshold was chosen arbitrarily).

A divergent pixel that was only identified in one of the two dark frames is flagged as an "anomalous" pixel for the dark frame affected. To prevent this anomalous pixel to contaminate all "science" measurements during the DC removal process, its value is replaced by the median value M(r) for the corresponding row.

Anomalous pixels: The method for their detection is similar to the method used for the detection of hot pixels but instead performed in the "science" measurements after the DC removal. Contrarily to dark frames, the illumination of the CCD varies both horizontally and vertically in a "science" frame (see Fig. 2). The detection is divided into three steps, each step corresponding to a part of the CCD that has similar illumination. The three parts are, 1) the LR, 2) The NLR below the LR and 3) the NLR above the LR (see Fig. 2).

As we can see in Fig. 6 c) and e) for the LR case, the spectra (=rows) do not have the same absolute values but show nonetheless a similar behavior. We therefore not use the absolute values of the recorded spectra to identify divergent pixels, but rather relative differences D(w,r) between adjacent pixels.

Using D(w,r), we calculate the vertical mean MD(w) and standard deviation StdD(w) on all the row pixels for each spectral pixel. Then an iterative process, similar to that explained above for the hot pixels detection, is applied: Identifying the divergent pixels using MD and StdD, which are both updated at each iteration by discarding from the mean and standard deviation recalculation all the divergent pixels identified at previous iteration. The equation to identify the divergent pixels is given by:

$$D(w,r) - MD(w) \; > \; k_{ano}\, StdD(w)$$

As for hot pixels, the number of iterations is typically between 2 and 4 and the k_{ano} factor (ranging between 2.5 and 6) were arbitrarily chosen, using a subset of observations at the beginning of the mission, by iterative tuning and visual approval of the noise removed spectra. An example for the LR of each viewing mode is given in Fig. 6. The set of values also depend on the type of measurements, with, as for hot pixel detection, more relaxed detection criteria for occultations, medium for nadir daysides and stricter criteria for limb and nightside observations.

4.5. Smearing removal

The smearing effect occurs because the CCD is still illuminated while being read row by row: The top rows, which are read after, can therefore receive more illumination than the bottom ones. As mentioned in Section 3.3.1, smearing does not affect occultation measurements for which the vertical truncation, applied before the reading, is large and directly shifts down the whole ROI in the bottom NLR of the CCD. On the contrary, nadir and limb measurements are affected by the smearing: a larger ROI combined with a less important truncation makes that the ROI is still partly illuminated during the reading, as explained in Section 3.3.2.

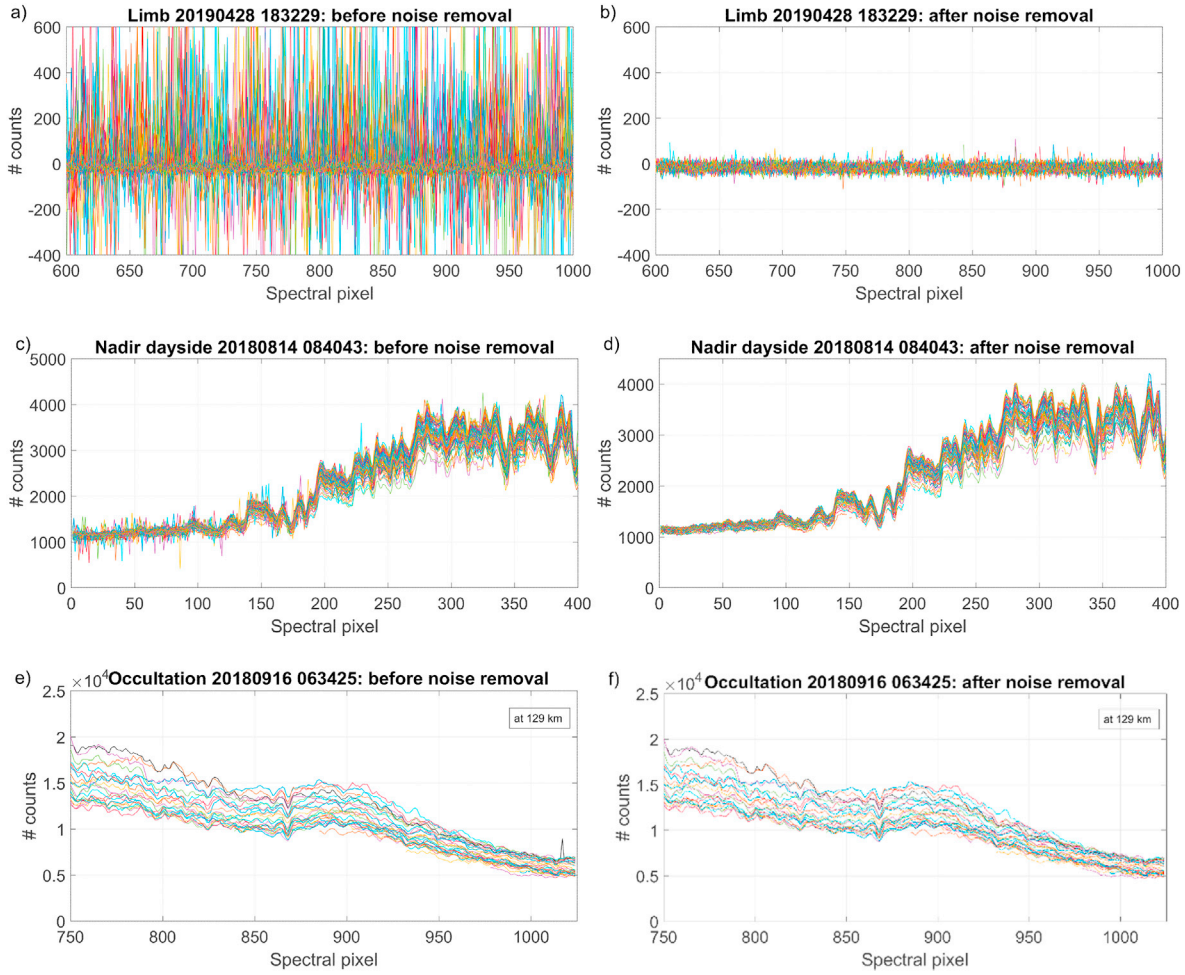

Fig. 6. Examples of bad pixel removal for a limb observation around 70 km altitude (a,b), for a nadir dayside (c,d) and for an occultation at 129 km (e,f). Spectra before bad pixel removal are displayed on the left and after removal on the right. The different lines on each plot represent the LR rows of a CCD frame. These plots show the importance of the noise removal, especially when signal is lower. Almost no signal is recorded in the limb measurement example (top). The little bump around pixel 793 in top right panel corresponds to the first detection of the green line at 557.7 nm [Gérard et al., 2020], which faint signal was completely drowned in the noise at first (top left). Many "spikes" are still identified in the nadir measurement (middle). One "spike" was found in the occultation case.

For limb and nadir measurements, the smearing must be removed from each CCD frame. If all the 256 CCD rows were read, the signal of a CCD row would be composed of the signal recorded by this row during the integration time (IT, usually 5–20 s) added to the signal acquired during the readout process, corresponding to the sum of the 0.01 s contributions spent on each row below. In this case, the r-th row (r in [1:256]) of the frame corrected for smearing Y_{SC} is obtained by subtracting the cumulative smearing corrections (SC):

$$Y_{SC}(w,r) = Y_{DC}(w,r) - \sum_{r_j=0}^{r-1} SC(w,r_j) \quad (2)$$

where the smearing correction of a given row r_j is calculated as:

$$SC(w,r_j) = \frac{0.01}{IT} Y_{SC}(w,r_j)$$

The SC terms is calculated row by row recursively: starting from row 1 that does not contain smearing SC(w,0) = 0. From there, SC(w,1) can be calculated and used to correct row 2, which allows to calculate SC(w,2) to correct row 3, and so on recursively until the whole CCD is corrected.

In practice, only a part of the CCD is read, e.g. in the case of Fig. 7, we consider a ROI of 194 rows with a starting row (r_0) at row 48. Equation (2) here above must be adapted to take into account of the truncation and the fact that the value of the smearing correction for the first rows below r_0 is not known. The impact of the SC of these first rows are relatively limited as they are lying in a non-illuminated part of the CCD that only contains little straylight, and which corrections have been estimated. A study of the SC in the non-illuminated area was performed using full frame measurements (i.e reading all 256 rows) specifically recorded during the mission for this calibration purpose. The study has shown that the SC increases gradually with the row number and can be estimated as a fraction of another non-illuminated row. Row number 100 is used as reference to calculate the SCs of these first rows (Row 100 was chosen because it is the last row fully contained in the NLR, with therefore a larger straylight and a lower relative error than the rows below). Taking the truncation into account, Equation (2) for smearing correction given above is changed to:

$$Y_{SC}(w,r) = Y_{DC}(w,r) - \sum_{r_j=0}^{r-r_0} SC(w,r_j)$$

where r is the ROI row number considered (for Fig. 7 example, r = [48,241]). The same recursive procedure as described above can be applied. An example of the smearing correction for a vertical slice of the CCD and how the smearing increases as a function of the CCD row is shown in Fig. 7.

4.6. Wavelength assignment

An initial pixel to wavelength assignment was performed using laboratory measurements performed before launch in 2016. These measurements were obtained with Pen-Ray light sources (models: Hg–Ne #6034, Xe #6033, Ne #6032, Kr #6031, Ar #6030 from Newport®) that produce monochromatic emission lines at known wavelengths, the spectral output of the Hg–Ne Pen-Ray light source is shown in Fig. 8. The identification of these spectral lines allows the wavelength-pixel assignment to be derived. At the start of the science mission, the wavelength assignment was further improved, by comparing the position of the solar lines in UVIS measurements with a solar reference spectrum. The reference spectrum used for this is a high resolution spectrum coming from [Meftah et al., 2018], that was convoluted to UVIS resolution for the comparison. A small adjustment (<0.5 nm) was applied from the first

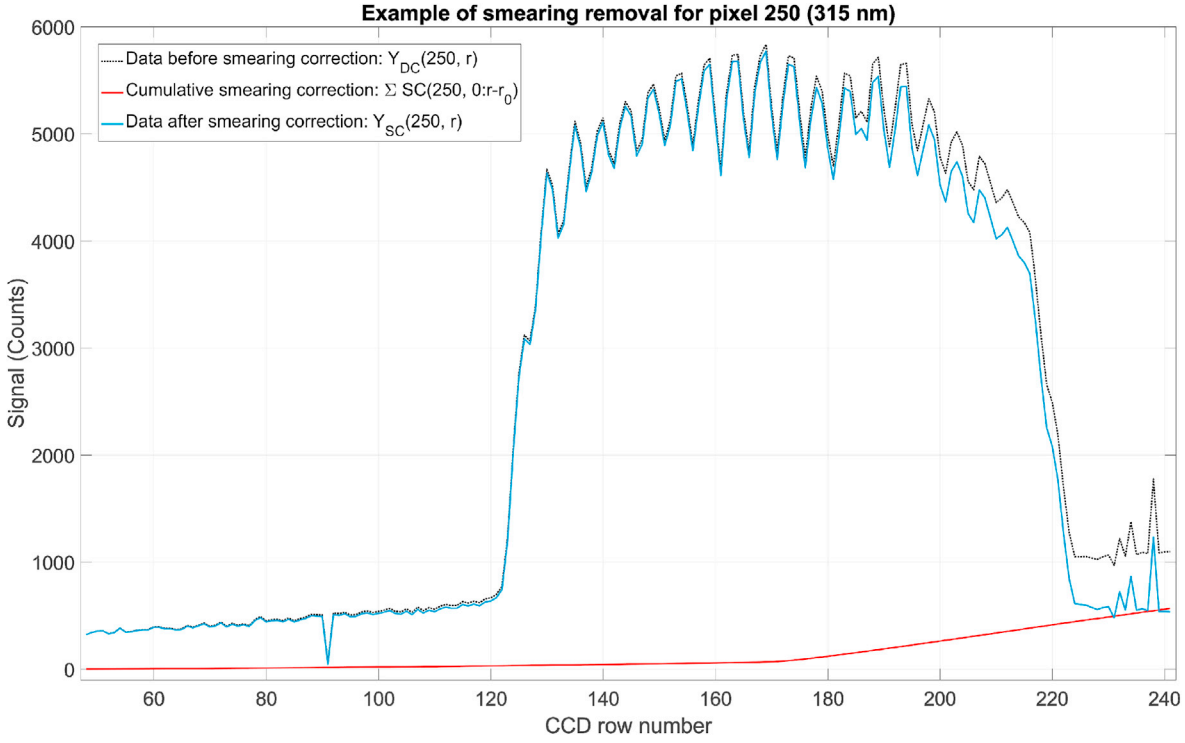

Fig. 7. Example of the smearing removal for a vertical slice of the CCD at spectral pixel 250 (around 315 nm) with a ROI between rows [48,241]. The data before and after the smearing subtraction are represented by the dotted black and solid blue lines respectively. The illuminated part of the CCD at this wavelength lies between rows 123 and 223, while outside of this region the signal is lower and originates from straylight. The cumulative correction for smearing is given by the red line. It shows a change of slope around row 170 (=123 + 47, i.e. the smearing shift due to truncation): below row 170 the smearing contributions are lower as they come exclusively from the non-illuminated part of the CCD, while above that row, contributions from the illuminated part are also added and becomes therefore more significant. Note that the periodic features present in the illuminated part of the CCD are due to the illumination of the 19 fibers. These features are also visible in the CCD frame of Fig. 2a.

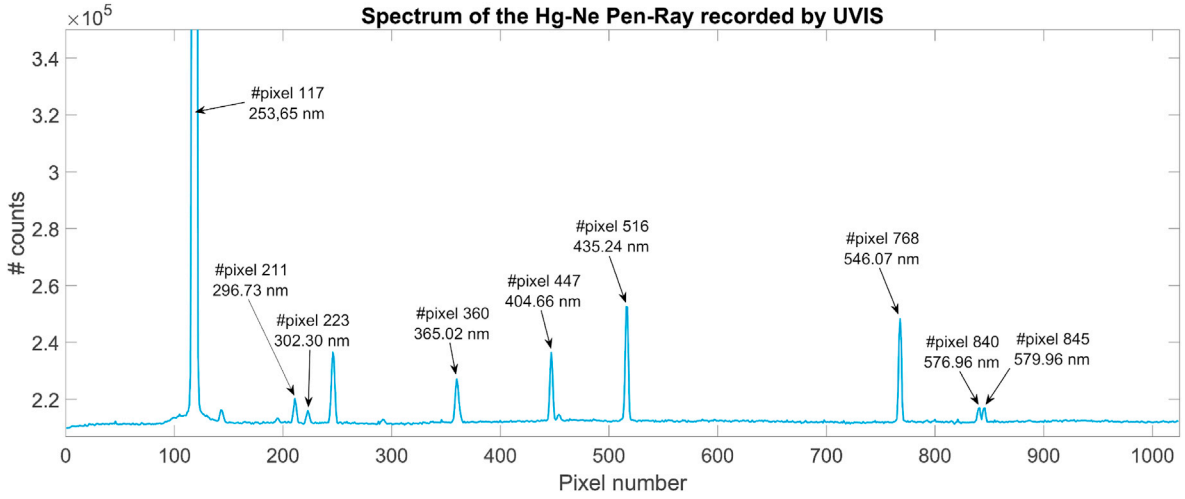

Fig. 8. Spectrum of the Hg–Ne Pen-Ray calibration lamp recorded by UVIS. The annotations provide the assignment with the known wavelength emission lines from the lamp.

wavelength assignment to optimize the match between UVIS in-flight solar measurements and the solar reference spectrum. The final pixel to wavelength assignment is shown in Fig. 9.

4.7. Straylight removal

As already mentioned, UVIS suffers from straylight contamination. The straylight was identified to originate partially from UV–visible light, i.e. within the UVIS range [200–650 nm], but predominately from the near infrared (NIR) between 650 and 1100 nm, outside of the UVIS range. The removal of the straylight is critical in the calibration process, especially in the UV and even more for dayside nadir measurements where the straylight level can be larger than the "true" observed signal. Two examples of UVIS spectra before and after straylight removal are shown in Fig. 10 to illustrate the importance of this process. Two completely independent methods were developed to remove the straylight.

One of the methods is based on the laboratory calibration measurements that identified the straylight contamination recorded on the UVIS proto-flight model (pFM) after delivery to the orbiter. An in-depth analysis of the straylight was pursued on the UVIS flight-spare (FS) model post launch. The resultant FS straylight correction was compared against the pFM straylight and showed the same general behaviour except for some small differences in intensity and features. The FS straylight correction was therefore adapted to take account the flight model differences so it could be applied to the pFM. The straylight was studied using band passes filters and different calibrated lamp sources emitting from the UV to the IR. This method allows the straylight to be estimated knowing the incoming NIR radiation reaching the instrument, with the NIR radiation simulated and extrapolated from the UVIS signal around 650 nm. This method is described in [Depiesse et al., In prep] and is applied to nadir dayside measurements.

The second method uses in-flight data from the non-illuminated part of the CCD to determine the straylight in the illuminated part. The NLR parts contain only straylight after the smearing removal and thus provides a direct measurement of the NLR straylight present at each wavelength for every measurement. A specific (spectrally variable) interpolation is performed between the top and bottom NLR to derive the straylight in the LR. This method, described in [Mason et al., 2022], is applied to all types of measurements (except for vertically binned data, where it is not possible) and is currently the nominal straylight removal method used in final data products.

A comparison of the two independent straylight removal methods' results is given in Fig. 11 for dayside nadir measurements. It compares the straylight results around 255 nm where ozone absorption is maximal (and in the UV where the straylight correction is critical). It shows that

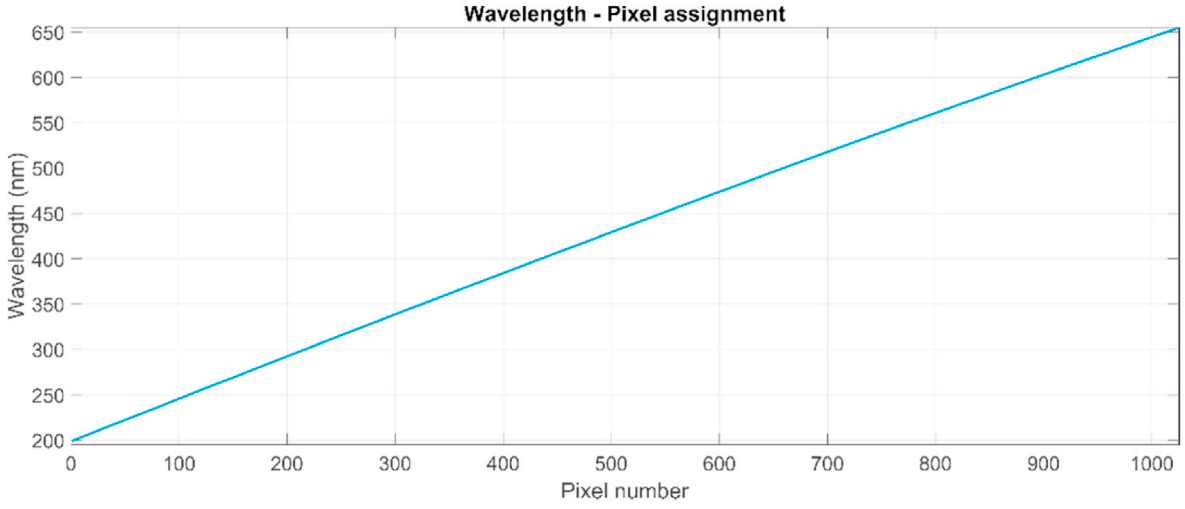

Fig. 9. Pixel to wavelength assignment for the 1024 effective pixels.

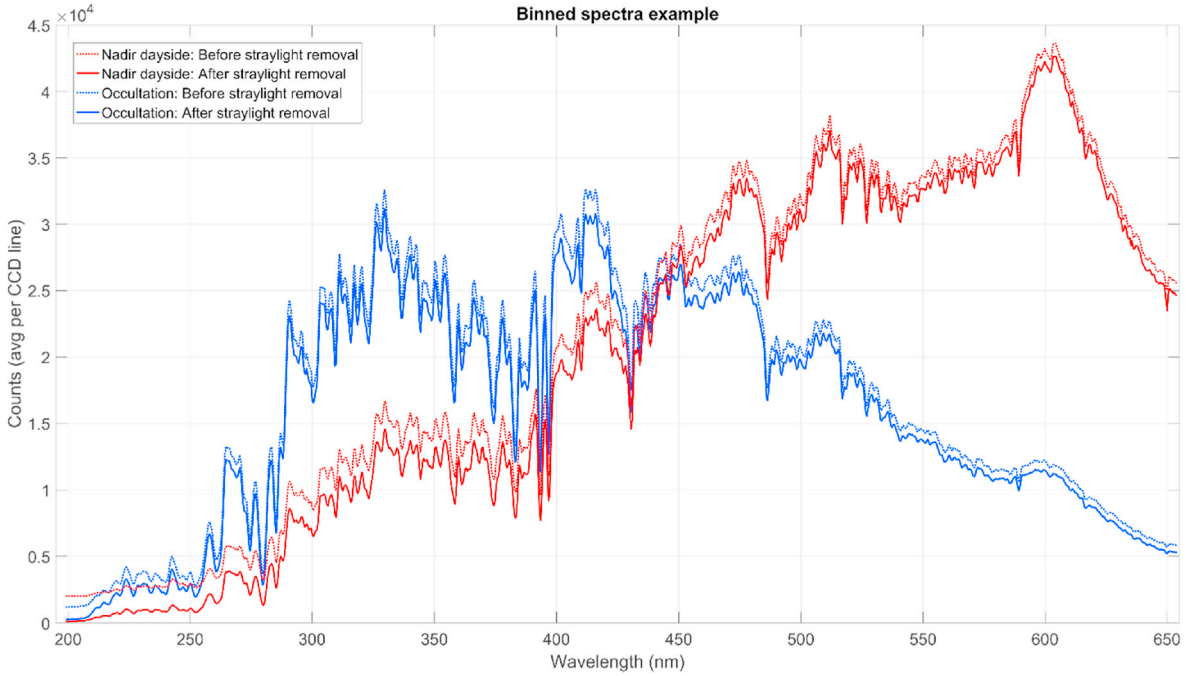

Fig. 10. Examples of binned spectra for an occultation in blue (20180916_063,425, observation 35 corresponding to 129 km altitude, same as Fig. 1b) and for a dayside nadir observation in red (20180814_084,043, observation 288, same as Fig. 1a). The x-axis is given as wavelength using the wavelength-pixel assignment described in Section 4.6. A comparison between the spectra before and after the straylight removal shows how critical this process can be for some parts of the spectra, as for instance in the UV, where the "true" signal is the lowest and where the straylight can reach the same level of signal or even larger (see the nadir observation below 260 nm).

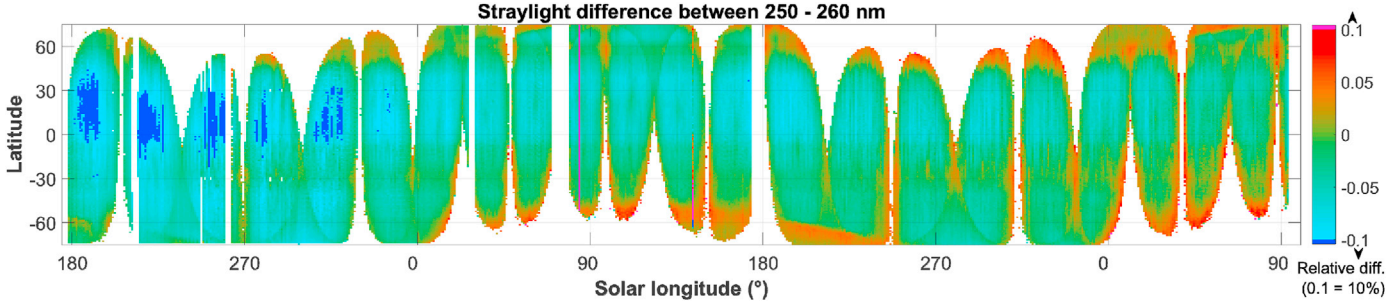

Fig. 11. Relative difference between the straylight estimation of the two methods between 250 and 260 nm for the period going from May 2018 to end of August 2021. The values < -10% are represented in dark blue and >10% in magenta.

the observed differences between the two methods generally lie within <10%. A more detailed analysis and comparison of the two methods' results is provided in the companion paper of [Depiesse et al., In prep]. The study of the straylight and its correction is critical to the UVIS science objectives, with ongoing monitoring and analyses continuing to improve both methods.

4.8. CCD vertical binning

The frame data are binned (added) to obtain one spectrum per measurement with an improved SNR. The binning region (BR) is defined inside of the LR part of the CCD and includes the most illuminated part of it. Two BR are therefore used, one corresponding to each channel (nadir or occultation). As the LR, the BR varies with the wavelength depending on the illumination.

In occultation, for a considered wavelength, the BR includes all row pixels having a signal larger than 70% of the maximum signal within the spectral pixel column. Similarly to the LR, the number of binned rows increases from the UV to the visible: it includes 7 rows around 200 nm (rows 171–177) to 32 rows around 650 nm (rows 152–183).

For the nadir channel, we used originally a constant 81 rows BR for all wavelengths but we noticed that some well illuminated rows of the UV were not taken into account with this setup. As the UV part is the most critical in terms of signal, we changed to a BR also variable with wavelength, adding some more rows in the UV and increasing therefore the SNR. A similar delimitation than for occultation was applied, including all row pixels having a signal larger than 60% of the maximum signal within the spectral pixel column. The number of binned rows includes 87 rows around 200 nm (rows 131–217) to 82 rows around 650 nm (rows 128–209).

Note that the bad pixel identification is taken into account during the binning process, discarding some of the identified bad pixels depending on the measurement type. For the nadir channel, all bad pixels (saturated, hot and anomalous pixels) are discarded prior to binning. The result is then normalized by the number of rows included in the binning to obtain an averaged signal per row. For occultation, only saturated and anomalous pixels are removed. However, one must keep in mind that occultation measurements are converted into transmittance, i.e. dividing all measurements within an observation by a reference measurement at the top of the atmosphere. Therefore, any pixel discarded in one

measurement must be removed from all measurements within the observation in order to keep the measurements comparable between themselves and to obtain an appropriate transmittance.

4.9. Radiance and transmittance conversion

The final step of the calibration is the conversion of the data into transmittance or radiance. Occultation observations are converted into transmittances and nadir/limb measurements into radiance units (W m^{-2} nm^{-1} sr^{-1}).

4.9.1. Occultation channel: transmittance conversion

The method used to calculate the transmittance in occultation observations was described in [Trompet et al., 2016]: it takes the measurements recorded above 120 km altitude to calculate a reference spectrum at the top of the atmosphere (TOA). Above that altitude, solar spectra with no atmospheric extinction are recorded. All the spectra recorded below this 120 km altitude are divided by the TOA reference spectrum, providing the relative extinction of the atmosphere as a function of tangent altitude. The obtained transmittance spectra are therefore self-calibrated and do not require an absolute calibration. The transmittance T(w,i) for the binned spectrum Y(w,i), which was also corrected for straylight is calculated as:

$$T(w,i) = \frac{Y(w,i)}{S(w)} \tag{3}$$

with S the TOA reference spectrum and can be calculated using different methods as described in [Trompet et al., 2016]. An example of UVIS transmittance spectra for an occultation observation is shown in Fig. 12.

4.9.2. Nadir/limb channel: radiance conversion

The nadir and limb observations do not have a solar reference measurement to perform a self–calibration, therefore, an absolute radiometric conversion is required. The radiometric calibration was obtained using laboratory measurements recorded with the pFM before launch. Because of some delay in the building of NOMAD, those measurements took place at the Centre Spatial de Liège during the thermal and vacuum tests before integration into the satellite. This gave the opportunity to verify the radiance and wavelength calibration as a function of temperature of the spectrometer in vacuum. Except for the DC, the UVIS calibration, and more specifically the CCD detector, has shown no dependency on the instrument temperature. Measurements of three different lamp sources with a known and calibrated radiometric response were performed, these three separate lamps were required to ensure full coverage of the UVIS spectral range. The measurements were repeated ten times for each lamp. The full pipeline process, described in Sections 4.1 to 4.8, was applied to each lamp measurement, then averaged over the ten measurements for a given lamp in order to be used for the radiance conversion calculation. The resulting calibrated spectra in counts are shown in Fig. 13a and the derived radiance conversion curve in Fig. 13b.

The RS12 lamp, by Gamma Scientific® is a NIST Traceable sources that can be used as white light standards of spectral radiance or luminance (2.5% uncertainty); it is composed of a tungsten-halogen lamp and a diffuser. The size of the RS12's diffuser fully covers the acceptance cone of the nadir field of view. It served as the absolute reference to derive the count-to-radiance (CTR) curve between 429 and 650 nm. The CTR curve was obtained by taking the ratio of the radiance from the calibration certificate multiplied by the integration time (IT) and divided by the measured count number from the lamp spectrum.

The two other NIST calibrated lamps used to determine the CTR on the rest of the spectral range, were calibrated in irradiance and did not include a diffuser. As the nadir telescope includes a parabolic mirror and a fiber bundle, it is therefore not compatible with a point source illumination (or a quasi-point source like the filament of a bulb) and the source must fill the full field of view of UVIS. A diffuser was used to homogenize the radiation source, however, by adding a diffuser we could no longer rely on the calibration certificate of the lamps. The diffusing properties of the diffuser were measured in the lab in the same conditions (lamps and distances). We therefore used a relative approach to estimate the absolute radiometric quantities.

A 1000 W tungsten-halogen lamp from Osram Sylvania® (model T6, 3% uncertainty), called hereafter “W lamp”, was used to calculate the CTR curve between 372 and 429 nm. Knowing the radiance conversion at 429 nm from the RS12 lamp, we derived the radiance of the W lamp at this particular wavelength by calculating the scaling factor between the

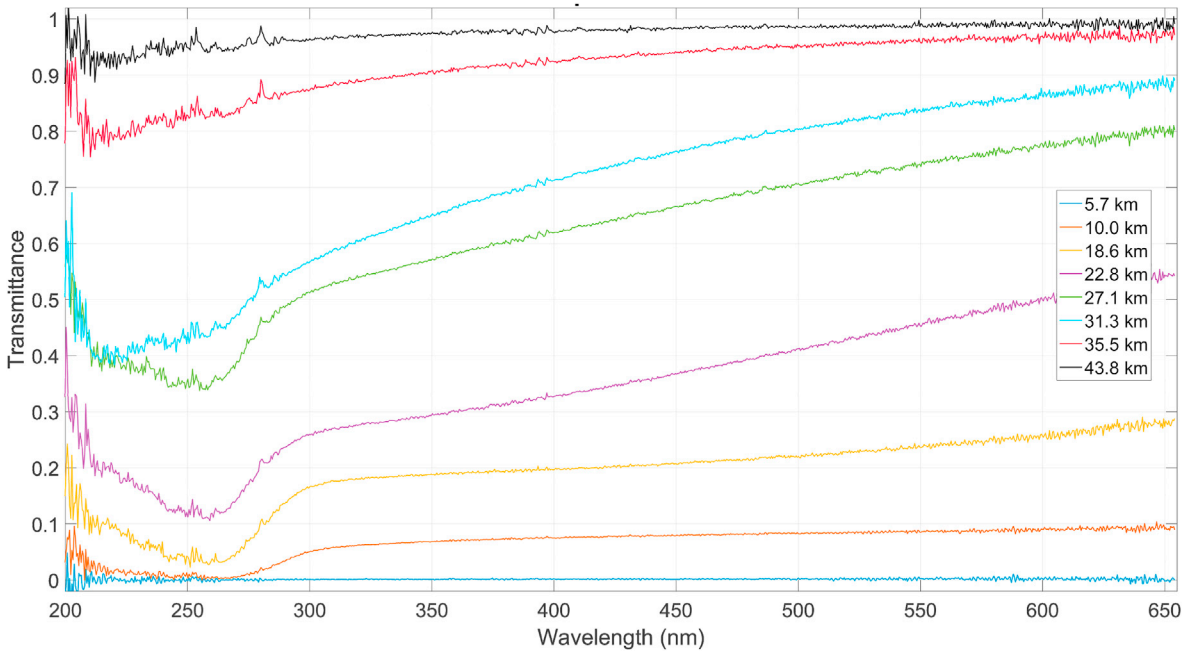

Fig. 12. Examples of transmittance spectra recorded at different altitudes for the occultation observation 20180426_141,656. The characteristic absorption feature of ozone Hartley band is recognizable between 220 and 290 nm below 30 km.

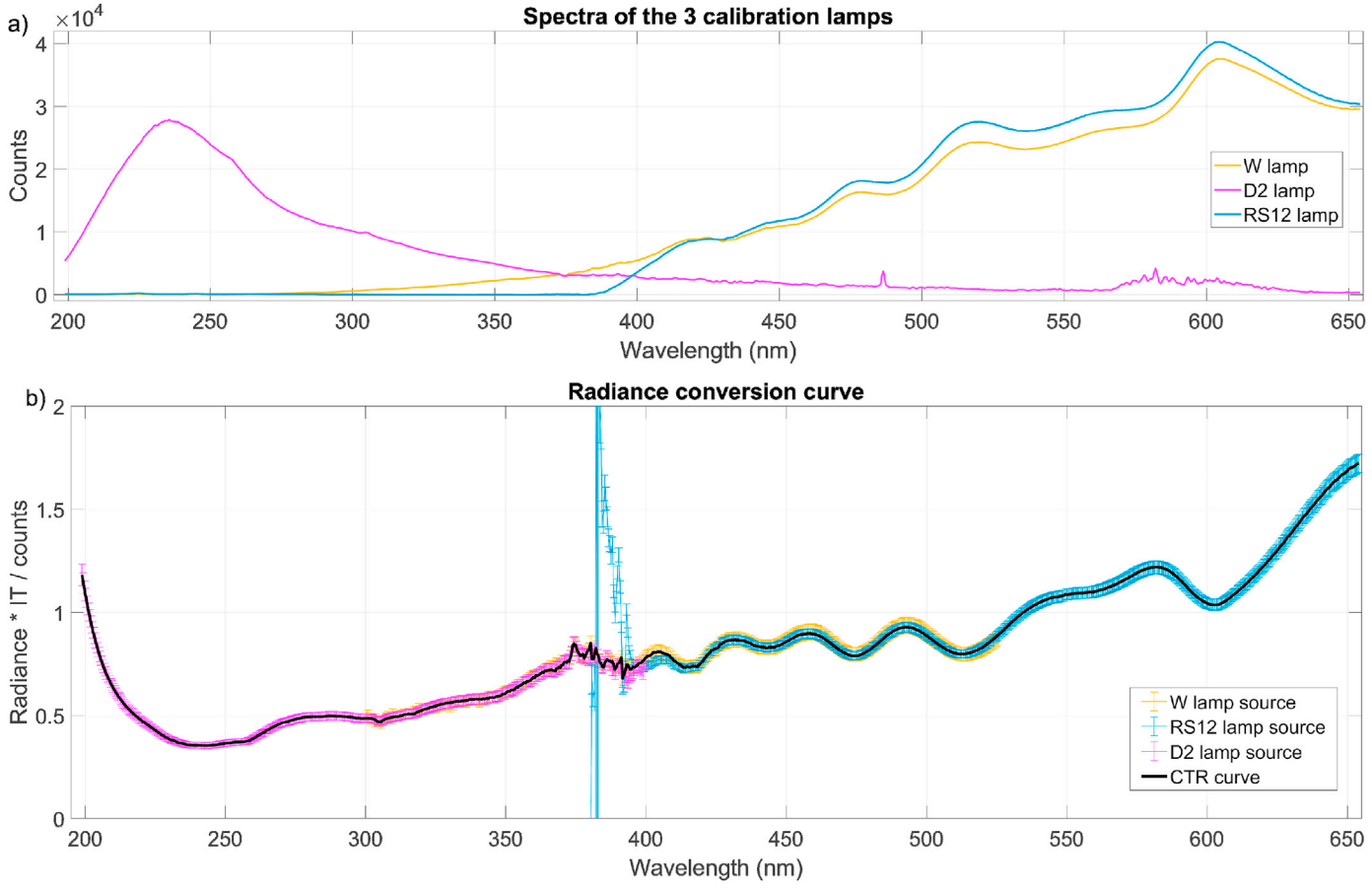

Fig. 13. a) UVIS spectra of the 3 lamps used for the determination of the radiance conversion for the nadir/limb channel. b) Count-to-radiance (CTR) curve derived using the 3 lamps (black line). The curves derived for each lamp are given by the colored lines with their associated error. The ordinate axis refers to a radiance given in μW cm^2 sr^{-1} nm^{-1} and an IT in ms.

two: the scaling factor was obtained by taking the ratio of the two RS12 and W spectra (in count/s). The extrapolation of the radiance to the other wavelengths down to 372 nm was performed by scaling the irradiance radiometric certificate of the W lamp with the scaling factor.

Below 372 nm, a 30 W deuterium lamp (model L6310 by Hamamatsu®, 1% uncertainty) was used. The same method was used for the deuterium (D2) lamp by scaling the radiance at 372 nm using the now-known (rescaled) W radiance at that wavelength. We took into account the UV absorption by the air in the optical path of the light between the lamp source and the vacuum chamber containing UVIS.

The final "binned" CTR is given in Fig. 13b with the contribution from each lamp. In practice, the CTR is calculated for each CCD row in the LR as this allows for a unique CTR to be calculated for each UVIS nadir (or limb) measurement by removing the equivalent bad pixels from the CTR prior to binning.

An example of radiance converted nadir measurements is shown in Fig. 14a. The radiance plot contains the solar lines and the spectrum intensity increases by more than two orders of magnitude between UV and visible wavelengths, making this representation sub-optimal to highlight the desired atmospheric features. Fig. 14b gives the same spectra but converted into radiance factor $R_f = \pi \frac{I}{F}$, where I is the measured radiance by UVIS and F is the incident solar irradiance at the top of the atmosphere (in the present case, the F used comes from "TSIS" public database which provides daily Solar measurements[2]). Note that Fig. 14b is only given to emphasize the atmospheric features, the radiance factor product is not provided in the UVIS data files.

4.10. Error and uncertainty

This section gives the details of the errors available in the UVIS files that are calculated along the different calibration steps.

4.10.1. "Random" error

We provide the so-called "random" error dataset associated to each pixel frame $Y_{DC}(w,r)$ after the DC removal. It is composed of three different sources: the shot noise (SN), the readout noise (RN) and the dark current (DC) removal error. The unbinned random error (Err_{RdmU}) is calculated as follows:

$$Err_{RdmU}(w,r) = \sqrt{Err_{SN}(w,r)^2 + Err_{RN}{}^2 + Err_{DC}(w,r)^2}$$

with

$$Err_{SN}(w,r)^2 = \frac{Y(w,r)}{G}$$

$$Err_{RN}{}^2 = \frac{(\ std(\ Ybias1 - Ybias2\ )\ )^2}{2}$$

[2] The "TSIS" database is publicly available on the LASP website (https://lasp.colorado.edu/lisird/) and provides daily solar measurements, covering the UVIS range, recorded by the Spectral Irradiance Monitor (SIM) [Harder et al., 2005]. Practically, to calculate the R_f, both I and F had to be convoluted to take account of each other's variable spectral resolution.

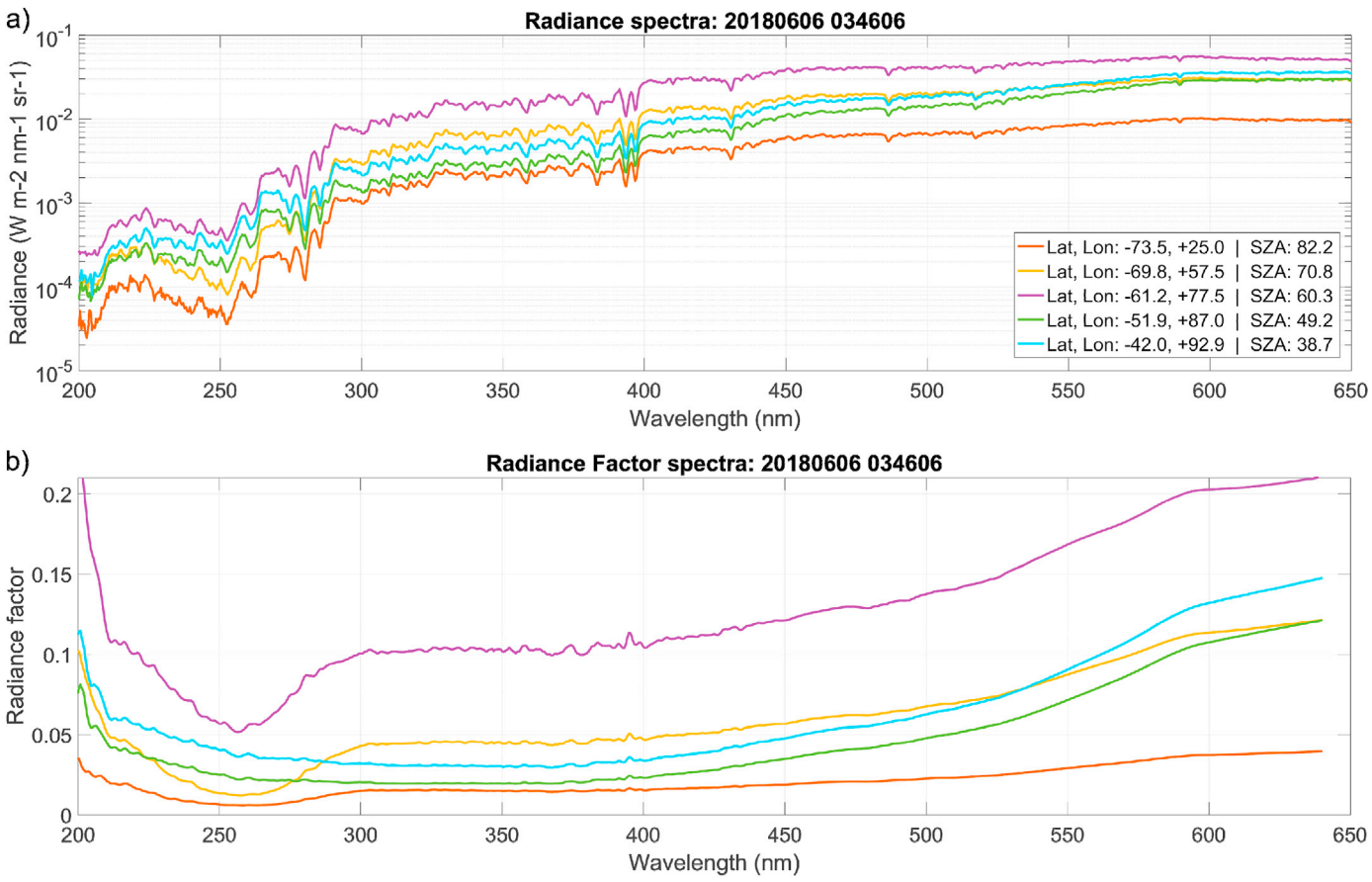

Fig. 14. a) Example of radiance converted nadir spectra. Note the intensity difference between UV and the longer wavelength region that can reach more than 2 orders of magnitude. b) Same spectra as in the top panel but given as radiance factors. The characteristic absorption feature of the ozone Hartley band is visible between 220 and 290 nm at the polar latitudes below 60°S as expected at this period (Ls = 188.3°) [Willame et al., 2017].

$$Err_{DC}(w,r)^2 = \sum_{X_j}\left(\frac{\partial Y_{dark}(w,r)}{\partial X_j}\right)^2 \Delta X_j^2$$

The shot noise is calculated using the gain G of the CCD. The read noise is calculated using the standard deviation on all pixels (w and r) of the bias difference frame; and the dark current error is calculated using the partial derivatives of Equation (1), where X_j can stand for Y_{darkP}, Y_{darkN}, $T_{fit}(m_{dark1})$, $T_{fit}(m_{dark2})$ or Tfit(m).

As the data are then vertically averaged on all the rows of the well-illuminated region of the CCD, the binned random error becomes:

$$Err_{Rdm}(w) = \frac{\sqrt{\sum_r Err_{RdmU}(w,r)^2}}{N_r(w)}$$

where N_r is the number of row included in the binning. It varies with w by taking into account the bad pixels removed and the CCD rows selected as valid data.

4.10.2. "Systematic" error

Another error dataset called "systematic" is calculated within the pipeline. It includes the errors due to the straylight removal (Err_{Sl}, for all types of measurement), the smearing correction (Err_{SC}, for nadir/limb only) and the radiance conversion (Err_{Rad}, for nadir/limb only).

$$Err_{Sys}(w) = Err_{Sl} \text{ for occultation}$$

$$Err_{Sys}(w) = \sqrt{Err_{Sl}(w)^2 + Err_{SC}(w)^2 + Err_{Rad}(w)^2} \text{ for nadir/limb}$$

The straylight correction is not discussed in this paper. For the "lab" method [Depiesse et al., In prep], the error is calculated from the same experimental steps used to estimate the straylight. For the "in-flight" method [Mason et al., 2022], an error quantification is not possible due to the nature of the method. It was estimated by comparison with the results of the lab method error and set arbitrarily to a conservative value of 5% of the total straylight. However, this still requires further analysis for improvement.

The smearing correction error is calculated similarly as the smearing removal process described in Section 4.5, and using cumulative terms of the unbinned random error:

$$Err_{SC}(w,r)^2 = \frac{0.01}{IT}\sum_{r_j=0}^{r-r_0} Err_{RdmU}(w,r_j)^2$$

The radiance conversion error was estimated from the experimental process described in Section 4.9.2 and are displayed through the error bars in Fig. 13b. This includes the uncertainties of the whole experimental set-up (lamp radiance, mirrors, windows, diffuser measurements) but also the uncertainties due to the calibration process, as the measurements follow all the calibration steps (from offset to straylight removal) before being used to determine the radiance conversion.

The "total" error dataset regroups the "random" and "systematic" error contributions, it is calculated from the quadratic sum:

$$Err_{Tot}(w) = \sqrt{Err_{Rdm}(w)^2 + Err_{Sys}(w)^2}$$

Fig. 15 shows an example of the random and total errors for a nadir observation. The total error usually represents around 3–4% in the visible range and becomes larger in the UV with values generally comprised between 5 and 15% (above 220 nm). Note that the three error datasets

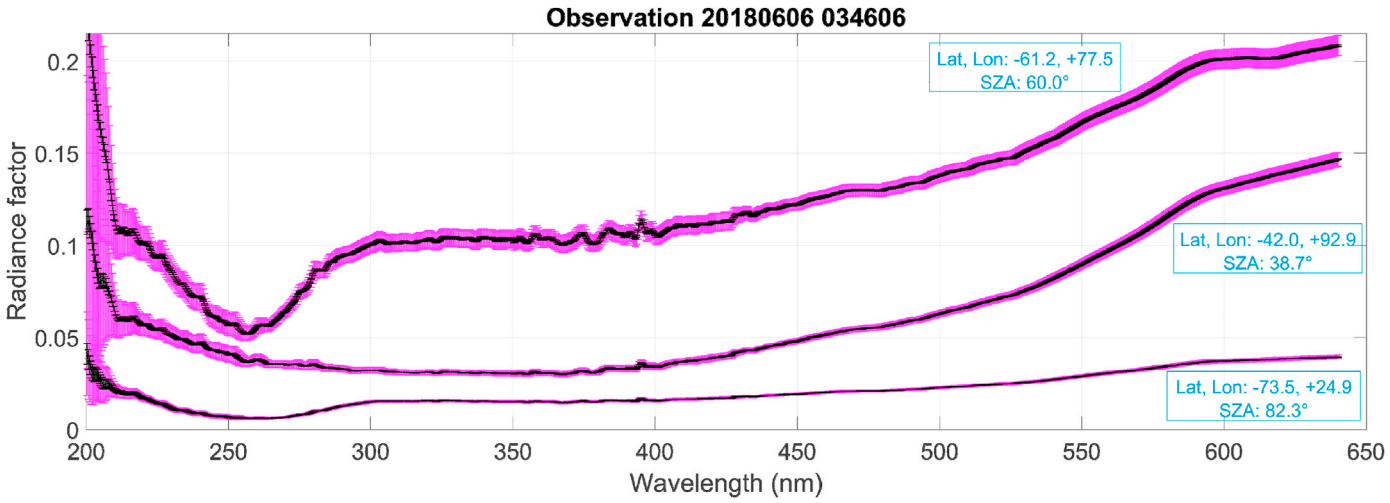

Fig. 15. Example of nadir spectra in radiance factor with errors (same observation as in Fig. 14). The black curve shows the transmittance error from "random" error while the purple curve is the "total" error.

(random, systematic and total) are available separately in the data files for science analysis purposes.

4.10.3. Transmittance error

The occultation error is obtained from the partial derivatives of Equation (3) in Section 4.9.1 and is calculated as:

$$Err_T(w,i) = \frac{\sqrt{Err_{Tot}(w,i)^2 + T(w,i)^2\, dS(w)^2}}{S(w)}$$

with dS the total error associated to the TOA reference spectrum S. See [Trompet et al., 2016] for more details about the calculation. Fig. 16 shows examples of occultation transmittance spectra with their associated errors. The total (relative) error is usually lower than 1% in the visible range and becomes larger in the UV, where the signal drops, and especially below 260 nm (cf. Fig. 10). It also increases as lower altitudes in the atmosphere are probed, due to the larger extinction of the signal. For instance, the relative error in the UV (220–300 nm) is typically 0.5–3% for the transmittance curve around 0.8 and can reach values between 5 and 20% for the transmittance curve below 0.2.

4.11. Instrument ageing

The ageing of any spatial instrument must be taken into account, especially in the UV where the photons are more energetic. To reduce this effect, UVIS's optical fibers were pre-solarized before the launch which decreased their transmittivity and stabilizes it for any further degradation.

In flight monitoring of the degradation can be performed with the occultation channel by analysing direct Sun measurements along the mission duration. From this analysis, a deterioration was observed reaching a decrease of some tens % for the recorded count rate in the UV around 250 nm. However, it is not an issue for the calculation of the transmittances as both the atmospheric measurements and the exo-atmospheric reference spectrum are affected by the same degradation, canceling the effect when taking the ratio (cf. Section 4.9.1).

For the nadir channel, the degradation would be an issue as it works with an absolute calibration. Fortunately, the UV incoming radiation is much less intense than in the occultation channel, making the degradation process much slower. Contrarily to occultation, we don't have any calibrated or characterized light source that can be used as a standard on flight. However, in the next section we show a radiometric comparison with coincident nadir measurements from MARCI. It provides an indirect

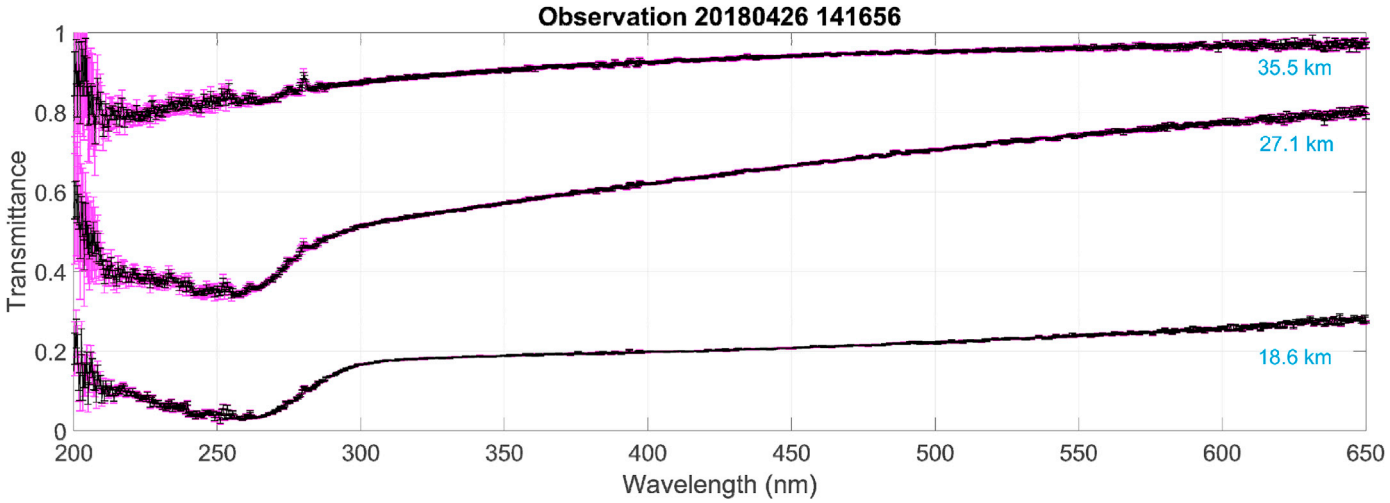

Fig. 16. Example of occultation spectra in transmittance with errors (same observation as in Fig. 12). The black curve gives the "random" error while the purple curve also includes the 5% straylight error (i.e. "total" error).

way to monitor the degradation of the UVIS nadir channel. The comparison does not emphasize any deterioration of the nadir channel (see next section for details).

5. UVIS-MARCI nadir comparison

To assess the validity of the calibration, we have performed a comparison of nadir measurements from UVIS with those obtained by the MARCI instrument [Bell et al., 2009]. The comparison is shown in Fig. 17 and uses paired "coincident" UVIS-MARCI measurements between May 2018 and December 2020 (MARCI measurements were obtained from [Wolff et al., 2010]). The paired observations considered here were recorded within 30 min, with a maximum of 60 km on the ground from each other and with the same geometry (difference of incidence angle $<1°$). This matching constraint is a balance between choosing the most similar matching pairs and keeping enough of them to have a good statistic for the comparison, with about 70 pairs comprising Fig. 17. For an appropriate comparison, the UVIS measurements were integrated using the band pass distribution of MARCI, that cover about 40 nm for the UV bands (6 and 7) and about 60 nm for the visible bands (1, 2 and 3).

One can see in Fig. 17 that the agreement between the two instruments is generally good, with differences mostly lying between $\pm$10%. A $\pm$ 10% difference seems to us a good confidence interval taking into account the individual measurement uncertainties of each instrument (typically, the uncertainty on MARCI's radiance varies between 1 and 10%), and the fact that the two instruments do not observe exactly the same scenery, in terms of time, location and/or viewing angle.

First, we should highlight the fact that the calibration is not very sensitive to the straylight removal in the visible range, on the contrary to the UV where it is critical. Indeed, as one can see from Fig. 10, the proportion of straylight in the visible is relatively limited in the visible and becomes more significant in the UV toward shorter wavelengths, where it can even be larger than the "true" signal itself. The impact can be seen in the comparison plots of Fig. 17: If we consider the visible ranges (bands 1, 2 and 3), we see that the calibration using the two straylight removal methods are (almost) identical. While for the UV (band 6 and 7), we can (sometimes) observe more marked differences between the results of the two methods. Both methods are generally in good agreement (as shown in Fig. 11 for the UV range around 255 nm). A more detailed comparison between the straylight removal results are provided in the companion paper of [Depiesse et al., In prep].

Bands 2 and 3 (550 and 600 nm) show a very good agreement between the two instruments with almost all points within $\pm$10%. While Band 1 shows also a good general agreement, with the majority of the points lying within the $\pm$10% range, but we observe a larger spread than for all others bands with several times differences between 10 and 20% and even larger for a few points (that reach up to 30%). The reason for the larger spread around 440 nm is still under investigation.

The results for band 7 around 320 nm also show a very good agreement with MARCI with almost all points included in the $\pm$10% for both methods and for which the results are usually very similar.

For band 6 around 260 nm, Fig. 10 shows how critical the straylight correction is at lower wavelengths. However, the agreement with MARCI is also good with most of the differences within $\pm$10%. Some points reach larger differences (10–30%) but are generally grouped together in Ls periods, which could suggest that the straylight removal correction may not be optimal for the illumination during these periods, and is still under investigation for improvement.

As mentioned in the previous section, the present comparison with MARCI measurements is also an indirect way to monitor the degradation of the nadir channel along time. The fact that UVIS results remain usually within 10% from MARCI's radiance during the whole covered period tends to show that no significant degradation is observed for the nadir channel from the beginning of the mission until January 2021. The comparison will be extended in time in order to monitor the degradation later in the mission.

6. Conclusion

We presented in this work the calibration process applied to UVIS data. The raw data undergo a series of calibration steps:

1. Potential non-linearity correction (for pixels in the non-linear regime)
2. Offset bias subtraction;
3. Dark current removal based on the temperature of the CCD;
4. Wavelength-pixel assignment;
5. Bad pixel identification/removal, critical for the nadir channel measurements with low signal (especially for nightside and limb measurements);
6. Smearing removal;
7. Straylight calculation/removal, critical for the UV part of the spectrum. Two different and independent methods, called "lab" and "in-flight", can be applied for the nadir channel. For the occultation channel, only the in-flight method is applicable. The straylight removal methods were not described in the present paper but are described in detail in two companion papers: see [Mason et al., 2022] for the in-flight method and [Depiesse et al., In prep] for the lab method, which also includes a comparison between the results of the two methods. A brief comparison between the results of two methods was provided and shows generally similar results, allowing to validate each other's;
8. Vertical binning on the illuminated rows of the CCD to increase the SNR (using the noise pixel flag to discard bad pixels);
9. Transmittance conversion for the occultation channel. This conversion is relative and self –calibrated as the solar reference measurement used to divide all spectra is recorded for each observation;
10. Absolute radiance conversion is necessary for the nadir channel. The radiance conversion curve was calculated from laboratory measurements obtained before launch in 2015 from three calibrated/known light sources;

As a final validation of the full calibration, a radiometric comparison of coincident nadir measurements from the MARCI instrument aboard MRO was provided for MARCI's five band in the UV and visible between 260 and 600 nm. The comparison between the two instruments shows generally very good agreement validating the calibration. Yet, some sporadic divergences are still reported and under investigation (between the two straylight methods and between MARCI-UVIS) which may lead to future improvement in the process of the calibration.

The calibrated UVIS data are used by the NOMAD team for studying the Martian atmosphere and have already led to some research results: the first detection of the Oxygen green and red lines (at 557.7 and 630 nm) from dayglow on Mars [Gérard et al., 2020, 2021]; Improved altitude distributions of ozone [Khayat et al., 2021; Patel et al., 2021]; Climatologies of ozone, dust and ice clouds from nadir measurements [Mason et al., EPSC2021; Willame et al., EPSC2021].

Author statement

Y. Willame: Conceptualization, Methodology, Software, Validation, Investigation, Data curation, Writing, Ground calibration campaign; C. Depiesse: Conceptualization, Methodology, Software, Validation, Investigation, Reviewing, Ground calibration campaign; J.P. Mason: Investigation, Conceptualization (Straylight removal), Reviewing, Ground calibration campaign; I. R. Thomas: Investigation, Conceptualization, Methodology, Supervision, Validation, Software, Data curation, Project

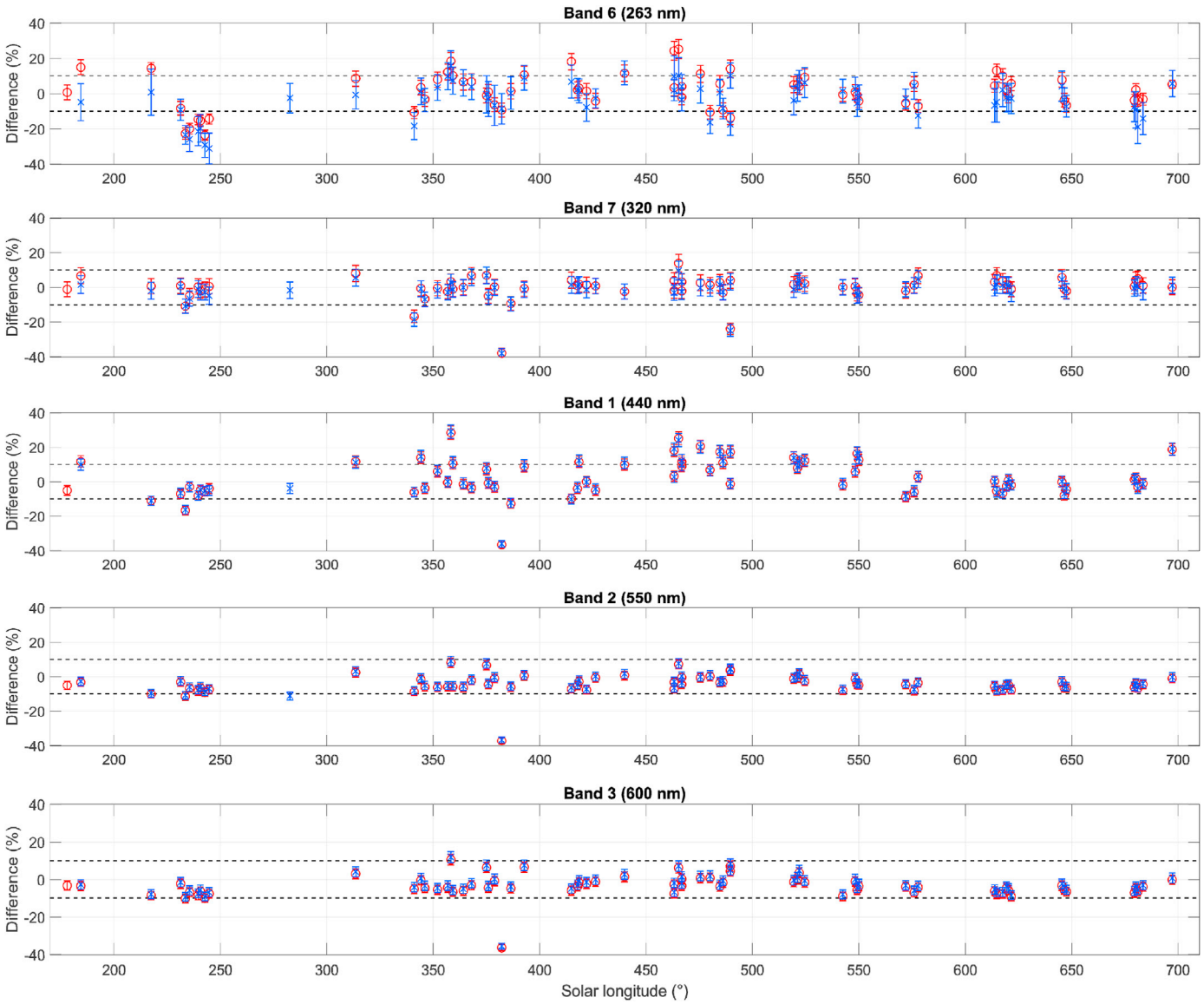

Fig. 17. Difference between calibrated UVIS and MARCI coincident measurements (MARCI's radiances from [Wolff et al., 2010]), i.e. recorded with the same geometry at the same location and time on the planet. The results of the two straylight removal methods are displayed by red circles for the "lab" method [Depiesse et al., In prep] and by blue crosses for the "in-flight" method [Mason et al., 2022]. The ±10% difference is indicated by the black dashed lines. Error on MARCI's radiance were not displayed for the clarity of the plots but are typically: 3–10% at 263 nm, 1–6% at 320 nm, 2–10% at 440 nm, and 1–7% at 550 and 600 nm.

administration, Reviewing, Ground calibration campaign; M. R. Patel: Investigation, Conceptualization (Straylight removal), Supervision, Reviewing, Ground calibration campaign; B. Hathi: Investigation, Ground calibration campaign; M.R. Leese: Investigation, Ground calibration campaign; D. Bolsée: Investigation, Ground calibration campaign support; M. Wolff: Investigation, Data curation (MARCI); L. Trompet: Investigation, Software, Reviewing; A.-C. Vandaele: Investigation, Conceptualization, Supervision, Project administration, Funding acquisition, Reviewing, Ground calibration campaign; A. Piccialli: Investigation, Reviewing; S. Aoki: Investigation; B. Ristic: Data curation, Investigation; E. Neefs: Investigation, Supervision, Ground calibration campaign; B. Beeckman: Software, Data curation; S. Berkenbosch: Software, Data curation, Ground calibration campaign; R. Clairquin: Software, Data curation, Ground calibration campaign; A. Mahieux: Investigation, Ground Calibration campaign, Reviewing; A. Mahieux: Investigation, Ground Calibration campaign, Reviewing; N. Pereira: Investigation; S. Robert: Investigation, Ground Calibration campaign, Reviewing; S. Viscardy: Investigation, Ground Calibration campaign; V. Wilquet: Investigation, Ground Calibration campaign; F. Daerden: Investigation; J.-J. Lopez-Moreno: Investigation, Supervision; G. Bellucci: Investigation, Supervision.

Declaration of competing interest

The authors declare that they have no known competing financial interests or personal relationships that could have appeared to influence the work reported in this paper.

Acknowledgements

The NOMAD experiment is led by the Royal Belgian Institute for Space Aeronomy (IASB-BIRA), assisted by Co-PI teams from Spain (IAA-CSIC), Italy (INAF-IAPS), and the United Kingdom (Open University). This project acknowledges funding by the Belgian Science Policy Office (BELSPO), with the financial and contractual coordination by the ESA Prodex Office (PEA 4000103401, 4000121493), by Spanish Ministry of Science and Innovation (MCIU) and by European funds under grants PGC2018-101836-B-I00 and ESP2017-87143-R (MINECO/FEDER), as

well as by UK Space Agency through grants ST/V002295/1, ST/P001262/1, ST/V005332/1 and ST/S00145X/1 and Italian Space Agency through grant 2018-2-HH.0. This work was supported by the Belgian Fonds de la Recherche Scientifique – FNRS under grant number 30442502 (ET_HOME). The IAA/CSIC team acknowledges financial support from the State Agency for Research of the Spanish MCIU through the 'Center of Excellence Severo Ochoa' award for the Instituto de Astrofísica de Andalucía (SEV-2017-0709). US investigators were supported by the National Aeronautics and Space Administration. Canadian investigators were supported by the Canadian Space Agency.

References

Bell III, J.F., Wolff, M.J., Malin, M.C., Calvin, W.M., Cantor, B.A., Caplinger, M.A., Clancy, R.T., Edgett, K.S., Edwards, L.J., Fahle, J., Ghaemi, F., 2009. Mars reconnaissance orbiter Mars color imager (MARCI): instrument description, calibration, and performance. J. Geophys. Res.: Planets 114 (E8).

Depiesse et al.. In preparation. Laboratory Straylight Analysis for NOMAD-UVIS and Comparison with In-Flight Reduction Method.

Gérard, J.C., Aoki, S., Willame, Y., et al., 2020. Detection of green line emission in the dayside atmosphere of Mars from NOMAD-TGO observations. Nat. Astron. 4, 1049–1052.

Gérard, J.-C., Aoki, S., Gkouvelis, L., Soret, L., Willame, Y., Thomas, I.R., et al., 2021. First observation of the oxygen 630 nm emission in the Martian dayglow. Geophys. Res. Lett. 48, e2020GL092334.

Harder, Jerald, Lawrence, George, Fontenla, Juan, Gary, Rottman, Woods, Thomas, 2005. The spectral irradiance monitor: scientific requirements, instrument design, and operation modes. Sol. Phys. 230 (1), 141–167.

Khayat, A.S., Smith, M.D., Wolff, M., Daerden, F., Neary, L., Patel, M.R., et al., 2021. ExoMars TGO/NOMAD-UVIS vertical profiles of ozone: Part 2: the high-altitude layers of atmospheric ozone. J. Geophys. Res.: Planets 126.

Mason, J., Patel, M., Holmes, J., Streeter, P., Brown, M., Sellers, G., Marriner, C., Lewis, S., Wolff, M., Willame, Y., Depiesse, C., Ristic, B., Thomas, I., Daerden, F., Vandaele, A.-C., López Moreno, J.J., Bellucci, G., 2021. The distribution of ozone on Mars as measured by the NOMAD-UVIS spectrometer in Mars year 34. Europlanet Sci. Congr. 13 (24 Sep 2021), EPSC2021–E2655.

Mason, J., Patel, M., Leese, M., Hathi, B., Willame, Y., Thomas, I., Wolff, M.J., Depiesse, D., Holmes, J., Sellers, G., Marriner, C., Ristic, B., Daerden, F., Lopez-Moreno, J.J., Bellucci, G., Vandaele, A.C., 2022. Removal of straylight from ExoMars NOMAD-UVIS observations. Planet. Space Sci. 105432, 0032-0633.

Meftah, M., Damé, L., Bolsée, D., Hauchecorne, A., Pereira, N., Sluse, D., Cessateur, G., Irbah, A., Bureau, J., Weber, M., Bramstedt, K., Hilbig, T., Thiéblemont, R., Marchand, M., Lefèvre, F., Sarkissian, A., Bekki, S., 2018. SOLAR-ISS: a new reference spectrum based on SOLAR/SOLSPEC observations. A&A 611, A1.

Neefs, E., Vandaele, A.C., Drummond, R., Thomas, I.R., Berkenbosch, S., Clairquin, R., Delanoye, S., Ristic, B., Maes, J., Bonnewijn, S., Pieck, G., 2015. NOMAD spectrometer on the ExoMars trace gas orbiter mission: part 1—design, manufacturing and testing of the infrared channels. Appl. Opt. 54 (28), 8494–8520.

Patel, M.R., Antoine, P., Mason, J., Leese, M., Hathi, B., Stevens, A.H., Dawson, D., Gow, J., Ringrose, T., Holmes, J., Lewis, S.R., 2017. NOMAD spectrometer on the ExoMars trace gas orbiter mission: part 2—design, manufacturing, and testing of the ultraviolet and visible channel. Appl. Opt. 56 (10), 2771–2782.

Patel, M.R., Sellers, G., Mason, J.P., Holmes, J.A., Brown, M.A.J., Lewis, S.R., et al., 2021. ExoMars TGO/NOMAD-UVIS vertical profiles of ozone: 1. Seasonal variation and comparison to water. J. Geophys. Res.: Planets 126, e2021JE006837.

Robert, S., Vandaele, A.C., Thomas, I., Willame, Y., Daerden, F., Delanoye, S., Depiesse, C., Drummond, R., Neefs, E., Neary, L., Ristic, B., Mason, J., Lopez-Moreno, J.-J., Rodriguez-Gomez, J., Patel, M.R., Bellucci, G., 2016. Expected performances of the NOMAD/ExoMars instrument. Planet. Space Sci. 124.

Trompet, Loic, Mahieux, Arnaud, Ristic, Bojan, Robert, Séverine, Wilquet, Valérie, Thomas, Ian R., 2016. Ann carine Vandaele, and jean-loup bertaux, "improved algorithm for the transmittance estimation of spectra obtained with SOIR/venus express. Appl. Opt. 55, 9275–9281.

Vandaele, A.C., Willame, Y., Depiesse, C., Thomas, I.R., Robert, S., Bolsée, D., Patel, M.R., Mason, J.P., Leese, M., Lesschaeve, S., Antoine, P., 2015. Optical and radiometric models of the NOMAD instrument part I: the UVIS channel. Opt Express 23 (23), 30028–30042.

Vandaele, A.C., Lopez-Moreno, J.J., Patel, M.R., et al., 2018. NOMAD, an integrated suite of three spectrometers for the ExoMars trace gas mission: technical description, science objectives and expected performance. Space Sci. Rev. 214, 80.

Willame, Y., Vandaele, A.C., Depiesse, C., Lefèvre, F., Letocart, V., Gillotay, D., Montmessin, F., 2017. Retrieving cloud, dust and ozone abundances in the Martian atmosphere using SPICAM/UV nadir spectra. Planet. Space Sci. 142, 9–25.

Willame, Y., Mason, J., Vandaele, A.C., Erwin, J., Piccialli, A., Depiesse, C., Wolff, M.J., Daerden, F., Thomas, I.R., Ristic, B., Patel, M.R., Bellucci, G., Lopez-Moreno, J.-J., 2021. Nadir retrieval of ice clouds and dust from NOMAD/UVIS on board Exomars TGO. Europlanet Sci. Congr. EPSC2021–E2715, 13–24 Sep. 2021.

Wolff, M.J., Clancy, R.T., Goguen, J.D., Malin, M.C., Cantor, B.A., 2010. Ultraviolet dust aerosol properties as observed by MARCI. Icarus 208 (1), 143–155.